



HAL
open science

The 2018-ongoing Mayotte submarine eruption: Magma migration imaged by petrological monitoring

Carole Berthod, Etienne Médard, Patrick Bachèlery, Lucia Gurioli, Andrea Di Muro, Aline Peltier, Jean-Christophe Komorowski, Mhammed Benbakkar, Jean-Luc Devidal, Jessica Langlade, et al.

► To cite this version:

Carole Berthod, Etienne Médard, Patrick Bachèlery, Lucia Gurioli, Andrea Di Muro, et al.. The 2018-ongoing Mayotte submarine eruption: Magma migration imaged by petrological monitoring. *Earth and Planetary Science Letters*, 2021, 571, pp.117085. 10.1016/j.epsl.2021.117085 . hal-03353428

HAL Id: hal-03353428

<https://uca.hal.science/hal-03353428v1>

Submitted on 24 Sep 2021

HAL is a multi-disciplinary open access archive for the deposit and dissemination of scientific research documents, whether they are published or not. The documents may come from teaching and research institutions in France or abroad, or from public or private research centers.

L'archive ouverte pluridisciplinaire **HAL**, est destinée au dépôt et à la diffusion de documents scientifiques de niveau recherche, publiés ou non, émanant des établissements d'enseignement et de recherche français ou étrangers, des laboratoires publics ou privés.



Distributed under a Creative Commons Attribution 4.0 International License

22

23

24 **Highlights**

25

- 26 - Lavas erupted offshore Mayotte since May 2018 are evolved basanites (~5 wt% MgO).
- 27 - The eruption is fed by a deep (> 37 km) mantle reservoir.
- 28 - Primitive magma has undergone at least 50% of crystallization in a $\geq 10 \text{ km}^3$ mantle
29 reservoir.
- 30 - Magma transfer rate show that the eruption is steadily supplied from the deep mantle
31 reservoir.
- 32 - After May 2019, ascending magma intersected a more evolved and shallower magma
33 reservoir.

34

35 **Keywords:** Mayotte, submarine eruption, dredges, petrological model, mantle reservoirs,
36 multiple storage zone

37

38

39

40

41

42

43 **Abstract**

44

45 Deep-sea submarine eruptions are the least known type of volcanic activity, due to the
46 difficulty of detecting, monitoring, and sampling them. Following an intense seismic crisis in
47 May 2018, a large submarine effusive eruption offshore the island of Mayotte (Indian Ocean)
48 has extruded at least 6.5 km³ of magma to date, making it the largest monitored submarine
49 eruption as well as the largest effusive eruption on Earth since Iceland's 1783 Laki eruption.
50 This volcano is located along a WNW-ESE volcanic ridge, extending from the island of Petite
51 Terre (east side of Mayotte) to about 3,500 m of water depth. We present a detailed petrological
52 and geochemical description of the erupted lavas sampled by the MAYOBS 1, 2, and 4 cruises
53 between May and July 2019 and use these to infer characteristics and changes through time for
54 the whole magmatic system and its dynamics from the source to the surface. These cruises
55 provide an exceptional time-series of bathymetric, textural, petrological, and geochemical data
56 for the 2018-2019 eruptive period, and hence bring an invaluable opportunity to better constrain
57 the evolution of magma storage and transfer processes during a long-lived submarine eruption.
58 Integrating the petrological signatures of dredged lavas with geophysical data, we show that the
59 crystal-poor and gas-rich evolved basanitic magma was stored at mantle depth (> 37 km) in a
60 large (≥ 10 km³) reservoir and that the eruption was tectonically triggered. As the eruption
61 proceeded, a decrease in ascent rate and/or a pathway change resulted in the incorporation of
62 preexisting differentiated magma stored at a shallower level. Magma transfer from the deep
63 mantle reservoir is syn-eruptive, as indicated by transfer times estimated from diffusion in
64 zoned olivine crystals that are much shorter than the total eruption duration. Our petrological
65 model has important hazard implications concerning the rapid and stealthy awakening of a deep
66 gas-rich magma reservoirs that can produce unusually high output rates and long-lived eruption.

67 Sudden tapping of large crystal poor reservoirs may be the trigger mechanism for other rarely
68 witnessed high-volume ($> 1 \text{ km}^3$) effusive events.

69

70 **1. INTRODUCTION**

71

72 The discovery in May 2019 of an active volcanic submarine edifice of exceptional size 50
73 km east of Mayotte island (Comoros Archipelago, Mozambique Channel, Fig. 1a) caused an
74 immediate mobilization of the French scientific community (Feuillet et al., 2019), and the
75 creation of the Mayotte Volcanological and Seismological Monitoring Network (ReVoSiMa,
76 2021). The eruptive site is located on the distal part of a 60 km long WNW-ESE volcanic ridge
77 that runs off the eastern flank of Mayotte, the subaerial expression of which is Petite Terre
78 Island (Fig. 1b). As of October 2020, this volcano had risen 820 m above the 3300 m deep
79 seafloor with an erupted lava volume of $\sim 6.5 \text{ km}^3$ (ReVoSiMa, 2021). This volume implies
80 exceptionally high time-averaged magma discharge rates ranging from 150 – 200 m^3/s (first
81 year), decreasing through 70 – 80 m^3/s (May–July 2019) to less than 35 – 45 m^3/s since August
82 2019 (ReVoSiMa, 2021). As such, it represents by far the largest monitored submarine eruption
83 (Carey et al., 2018; Chadwick et al., 2018, 2016; Clague et al., 2011; Perfit and Chadwick,
84 1998; Resing et al., 2011; Rubin et al., 2012) and the third largest mafic eruption of the last two
85 millennia after Eldgjá in 939 (Oppenheimer et al., 2018) and Laki in 1783-1784 (Thordarson
86 and Self, 1993), both in Iceland.

87 The seismo-volcanic crisis began in May 2018 with a series of strong tectonic
88 earthquakes, including 32 events with $M_w \geq 5$, located between 12 and 42 km depth, ~ 35 km
89 east of Mayotte (Cesca et al., 2020; Lemoine et al., 2020). On land, surface deformation

90 (subsidence and eastern motion) have been continuously observed since July 2018, and Very
91 Long Period (VLP) seismic events related to fluid migration and possible magmatic activity
92 have been occurring at least since mid-June 2018 (Cesca et al., 2020; Lemoine et al., 2020),
93 suggesting that the eruptive activity has been ongoing for more than two years. On-going
94 subsidence and seismicity have been linked to the eruption-related withdrawal of magma from
95 its storage zone (Cesca et al., 2020; Feuillet et al., 2020; Lemoine et al., 2020).

96 Three oceanographic cruises (MAYOBS 1, Feuillet, (2019), MAYOBS 2, Jorry, (2019),
97 MAYOBS 4, Fouquet and Feuillet (2019), Fig. 1c, d) between May and July 2019 provide an
98 exceptional time-series of bathymetric, textural, petrological, and geochemical data for the
99 2018-2019 eruptive period (Table 1). Since most mafic submarine eruptions are short-lived and
100 have only been sampled after the end of the eruption, their study provides little information on
101 their temporal evolution (Chadwick et al., 2018; Clague et al., 2018; Rubin et al., 2012). The
102 geographically and temporally well-characterized sampling performed during the MAYOBS
103 cruises thus brings an invaluable opportunity to better constrain the evolution of magma storage
104 and transfer during a long-lived submarine eruption. In this paper, we present a detailed
105 petrological, textural, and geochemical study of the submarine samples, to provide insights into
106 the temporal and spatial evolution of a large volume of gas-rich magma rapidly intruding the
107 lithosphere and reactivating multiple levels of magma storage. This is the first time that this
108 methodology, developed for subaerial eruption at monitored volcanoes (Di Muro et al., 2014;
109 Edmonds et al., 2013; Gansecki et al., 2019; Gurioli et al., 2018), and combining a large range
110 of petrological and geochemical approaches on a temporal series of lava samples, is applied to
111 a submarine eruption.

112

113 **2. GEOLOGICAL SETTING**

114

115 The Comoros Archipelago is located in the Mozambique Channel between the northern tip
116 of Madagascar and the eastern coast of Mozambique (Fig. 1a). The four islands which compose
117 the archipelago, Grande Comore, Moheli, Anjouan and Mayotte, are aligned on a NW-SE trend
118 (Tzevahirtzian et al., 2020). This trend is superimposed on a zone of active seismicity
119 connecting the northern extremity of Madagascar on the east, to the African coast to the west,
120 and several authors suggest the presence of a boundary between the Lwandle microplate and
121 the Somalia plate (Famin et al., 2020; Saria et al., 2014; Stamps et al., 2018). By combining a
122 structural study with stress inversion of earthquake focal mechanisms, Famin et al. (2020)
123 propose that this Lwandle and Somalian plate boundary is related to a complex E-W zone of
124 immature right-lateral wrenching of the lithosphere.

125 Despite numerous studies, the origin of the volcanism in this geodynamic context remains
126 a matter of debate (Bachèlery and Hémond, 2016; Class et al., 1998; Claude-Ivanaj et al., 1998;
127 Coltorti et al., 1999; Deniel, 1998; Flower, 1973; Michon, 2016; Nougier et al., 1986; Pelleter
128 et al., 2014; Strong, 1972; Thompson and Flower, 1971). Many hypotheses have been
129 formulated including the interaction of a mantle plume with oceanic lithosphere (Class et al.,
130 1998, 2005, 2009; Claude-Ivanaj et al., 1998; Emerick and Duncan, 1982; Hajash and
131 Armstrong, 1972) and the reactivation of lithospheric structures possibly in relation with the
132 East African Rift System (Lemoine et al., 2020; Michon, 2016; Nougier et al., 1986).

133 Trace elements and EM1 – HIMU isotopic signatures of volcanic rocks in the Comoros
134 Archipelago would support the interaction of a mantle plume with amphibole/phlogopite-
135 bearing oceanic metasomatized lithosphere (Bachèlery and Hémond, 2016; Class et al., 1998;
136 Pelleter et al., 2014; Späth et al., 1996). However, the mantle plume hypothesis is considered
137 incompatible with the migration of the African Plate towards the NNE and with the structural

138 features of the region (Famin et al., 2020). Finally, since the youngest volcanic activity occurs
139 both in Grande Comore (0.13 ± 0.02 Ma to present; Hajash and Armstrong, 1972; Emerick and
140 Duncan, 1982) with the active Karthala volcano (Bachelery et al., 2016) and in Mayotte (Cesca
141 et al., 2020; Feuillet et al., 2020; Lemoine et al., 2020; Zinke et al., 2003), the age progression
142 of volcanism is not consistent with formation of the archipelago by the migration of the Somali
143 plate over a fixed hotspot. Several lines of evidence suggest that the volcanism of the Comoros
144 archipelago is associated with lithospheric deformation rather than the result of a deep mantle
145 plume (Famin et al., 2020; Lemoine et al., 2020; Michon, 2016).

146 Mayotte, the easternmost island of the archipelago, southwestward of Anjouan (Fig. 1a), is
147 the oldest island with a maximum age of 20 Ma for the onset of subaqueous volcanic activity
148 (Debeuf, 2004; Emerick and Duncan, 1982; Hajash and Armstrong, 1972; Michon, 2016;
149 Nougier et al., 1986; Pelleter et al., 2014). It is composed of two main volcanic islands, Grande
150 Terre and Petite Terre, the latter located 4 km east of Grande Terre. Mayotte subaerial activity
151 is subdivided into multiple phases beginning in the southern part of Grande Terre (10.6 – 1.9
152 Ma) and then migrating towards the north (5 – 0.75 Ma) and the northeast (0.75 – Present)
153 separated by periods of quiescence (Debeuf, 2004; Nehlig et al., 2013; Pelleter et al., 2014).
154 The current volcanic activity takes place 50 km off Mayotte, on a WNW-ESE submarine
155 volcanic ridge on the east flank of the island, Fig. 1b, (Cesca et al., 2020; Feuillet et al., 2020;
156 Lemoine et al., 2020).

157

158 **3. METHODS**

159

160 *3.1. Sampling*

161 We first performed a high-resolution bathymetric survey of the eruptive site (Feuillet et
162 al., 2019, 2021) to identify strategic dredging sites. Erupted lavas were dredged on five sites,
163 each dredge running for about 100 – 600 m and returning a weight of approximately 300 – 900
164 kg (Fig. 1c). During three oceanographic campaigns (MAYOBS 1, Feuillet, (2019), MAYOBS
165 2, Jorry, (2019), MAYOBS 4, Fouquet and Feuillet (2019)), three dredges sampled the main
166 volcanic cone and the radiating ridges built before May 2019 (phase 1: DR01, DR10, DR12,
167 Table 1 and Fig. 1c, d), and two dredges on the S and SE flanks collected lava flows emitted
168 during a second phase in June 2019 (DR08) and July 2019 (DR11). We selected fresh samples
169 with representative morphologies and textures, including quenched pillow rims, pillow cores,
170 sediments, samples containing xenoliths and phenocrysts. For this paper, we focused our study
171 on glassy pillow rims that preserved the pre-quench textures, as well as xenoliths and
172 phenocryst-rich fragments.

173

174 3.2. *Analytical techniques*

175 Bulk rock compositions were obtained on a set of 10 samples from 5 dredges (DR0101,
176 DR0105, DR0801-ALF, DR080102, DR100511, DR11, DR1107(1), DR1107(2), DR110704-
177 b and DR120202, Suppl. material Table 1). Major elements were analyzed on a HORIBA-
178 Jobin-Yvon ULTIMA C ICP-AES at Laboratoire Magmas et Volcans (LMV, Clermont-
179 Ferrand, France). Trace elements were analyzed on an Agilent 7900 ICP-MS at Institut de
180 Physique du Globe de Paris (IPGP, Paris, France). In situ chemical analyses of minerals and
181 glasses were performed using the CAMECA SXFive Tactis electron microprobe at LMV.
182 Raman spectra were acquired on melt inclusions in olivine and magnetite, and on matrix glasses
183 at the Ludwig Maximilian University (LMU – Laboratory of crystallography) using an XPlora

184 One spectrometer (Jobin Yvon) coupled with an Olympus microscope at 100x magnification.
185 Details of the analytical procedures are presented in Supplementary Material “Methods”.

186 *3.3. Physical properties and textures*

187 Density measurements were performed on 27 lava samples using a Micromeritics
188 Geopyc 1360 envelope density analyzer, following the procedure detailed by Thivet et al.
189 (2020). The instrument measures the volume of particles with different sizes and shapes. These
190 density measurements lead to reproducible data with a maximum standard deviation of ± 30
191 $\text{kg}\cdot\text{m}^{-3}$ (1σ) on five repeated measurements. The porosity of the samples was then calculated
192 using vesicle-free rock density values (Houghton and Wilson, 1989) calculated from the partial
193 molar volumes of oxide components (Bottinga and Weill, 1970). Petrographic observations and
194 microtexture analysis were performed using optical microscope and scan. Vesicle and crystal
195 size distribution (VSD and CSD), vesicle and crystal number density (NV and NC), and vesicle
196 to melt ratio (VG/VL) were measured following the procedures in Shea et al. (2010) and
197 assuming a spherical shape for both vesicles and crystals (mostly olivine).

198 *3.4. Fractional crystallization model*

199 Back-crystallization models were performed to reconstruct a potential mantle-derived
200 parental melt. Equilibrium olivine and clinopyroxene were added in 1 wt % increments to the
201 bulk composition of sample DR0101 until the melt was in equilibrium with a Fo_{90} mantle
202 olivine. For each step, the composition of the equilibrium olivine was calculated from the
203 magma composition of the previous step assuming a K_d of 0.30 ($K_d = (\text{FeO}/\text{MgO})_{\text{olivine}} /$
204 $(\text{FeO}/\text{MgO})_{\text{melt}}$, Roeder and Emslie, (1970)) and a partition coefficient $D_{\text{Ni}} = (\text{Ni}^{\text{olivine}} / \text{Ni}^{\text{melt}} =$
205 $124 / \text{MgO} - 0.9$, Hart and Davis, (1978)). The composition of the equilibrium clinopyroxene
206 was calculated assuming a K_d of 0.28 (Putirka, 2008), oxides vs Mg# trends derived from a
207 series of unpublished clinopyroxene analyses in basanite samples from Mayotte (Hassen Ali,

208 2020), and $D_{Ni} = 2$. The proportions of olivine and clinopyroxene were adjusted to fit the trend
209 provided by a compilation of published bulk rock analyses from the Comoros Archipelago.

210 3.5. *Diffusion modelling*

211 Preliminary residence times were estimated using diffusion in zoned olivine crystals,
212 modelled with the DIPRA software (Girona and Costa, 2013). Reversely zoned olivine crystals
213 were oriented using an EBSD detector attached to a Zeiss Supra 55 VP field-emission scanning
214 electron microscope housed at IStEP (Paris, France). Electron microprobe analyses were
215 acquired along carefully selected profiles: we chose olivine crystals most likely to be cut close
216 to their center (large homogeneous core), and the shortest possible profiles, perpendicular to
217 euhedral faces and far from other faces, to avoid artificial lengthening of the profiles (e.g., Costa
218 et al. 2008, Couperthwaite et al. 2021). Fo profiles (Fo = atomic
219 $Mg/(Mg+Fe+Mn+Ca+Ni)*100$) were modelled using an average temperature of 1095 ± 20 °C,
220 an oxygen fugacity on the NNO buffer, and an arbitrary pressure of 200 MPa. Influence of
221 pressure on diffusion times is within uncertainty.

222

223 4. RESULTS

224

225 4.1. Petrological and geochemical features

226 Bulk rock compositions of the lavas from the eruptive site fall within the compositional
227 range of the moderately to slightly alkaline series of the Comoros archipelago, the “Karthala
228 trend” (Bachelery and Hémond, 2016; Class et al., 1998; Claude-Ivanaj et al., 1998; Coltorti et
229 al., 1999; Deniel, 1998; Flower, 1973; Nougier et al., 1986; Pelleter et al., 2014; Strong, 1972;
230 Thompson and Flower, 1971). They are silica-poor ($46 < SiO_2$ wt.% < 48 , Fig. 2a and Suppl.

231 material Table 1), and plot in the tephrite / basanite field of the TAS classification diagram.
232 Since their normative olivine content is $> 10 \%$ they will be referred to as basanites in this study,
233 although they are significantly evolved ($4.4 < \text{MgO wt.}\% < 5.3$), and different from mantle-
234 derived primitive basanites. Phase 2 lavas (DR08, DR11) are slightly more evolved than the
235 earliest erupted ones with MgO content spanning a narrow range from 4.4 – 4.6 wt.%. All lavas
236 analyzed are enriched in REE and other incompatible elements and display a steep chondrite-
237 normalized REE pattern, close to the upper range found in the older subaerial Mayotte lavas
238 (Fig. 2c).

239 Quenched samples are glassy, crystal-poor (4-6% crystals, Figs 3, 4, and Suppl. material
240 Tables 2 and 3), and contain significant amounts of vesicle-trapped volatiles ("popping rocks").
241 The average vesicularity of lavas is high, 35%, with a maximum of 43%, for phase 1 products
242 (DR01-DR10-DR12) collected on the ridges radiating from the main edifice. Phase 2 lavas,
243 collected on lava flows, are denser (average vesicularity of 31% for DR08, down to 18% for
244 DR11). Except for DR11, these values are much higher than vesicularities of typical MORB
245 popping rocks (Chavrit et al., 2014, 2012), but comparable with the few values measured for
246 submarine alkali basalts. The average vesicularity for all investigated samples is 27 %. Using
247 this average value, the 6.5 km³ of the new volcano are equivalent to 4.8 km³ of dense rock. Two
248 binary images of lava fragments from the two textural endmembers (the most and the least
249 vesicular lava) are shown in Fig. 3. DR0103a1 (Fig. 3b) from phase 1, is highly vesicular (43%)
250 and characterized by a homogeneous population of rounded vesicles with a mean size of 0.4
251 mm. The sample has a relatively high number of vesicles per unit of liquid (N_v , 17 mm⁻³). In
252 contrast, DR110704b (Fig. 3a) is characterized by a lower vesicularity than DR01, with big,
253 coalesced vesicles, up to 3 mm in diameter and a mean value of 0.8 mm and a drastic decrease
254 in small vesicles, that translate in a low N_v (0.1 mm⁻³). A general decrease in number of vesicles
255 is evident between the lava samples from phase 1 (DR01-DR10-DR12) and those from phase

256 2 (DR08-DR11), with DR11 samples being the lowest in terms of vesicularity and hence
257 inferred pre-eruptive gas content (Fig. 3c).

258 Crystals in all samples include coeval Fe-rich olivine (50 – 790 μm , $\text{Fo}_{69-73.5}$), Ti-
259 magnetite (50 – 100 μm), and apatite (< 20 μm , Fig. 4a, b). Rounded FeS droplets either
260 included in olivine and magnetite crystals or directly in the glass indicate the presence of
261 an immiscible sulphide liquid in some of the samples. Most crystals are euhedral, but skeletal
262 crystals of olivine and titanomagnetite (Fig. 4b) are present in all samples, providing evidence
263 for fast growth, likely linked to fast ascent rates. The small population of olivine phenocrysts,
264 > 0.4 mm (for phase 1 samples) and > 1 mm (for phase 2 samples), represents a very low
265 fraction of the total crystal population (0.3 – 1% of all olivine crystals). In samples from phase
266 2 (June 2019 – July 2019, samples DR08 and DR11), some of the olivine phenocrysts are
267 reversely zoned (Fo_{53} in the cores to Fo_{70} in the rims, Fig. 4c). Their rim composition is similar
268 to that of olivine microlites (Fig. 4a, b).

269 The June 2019 lava flow (sample DR080205) contains small mantle xenoliths (Fig. 4d,
270 e). The largest one (DR080205-x4) is ~5 mm in diameter, and composed of ~1 mm long crystals
271 of Fo_{90} olivine and orthopyroxene with a Mg# (atomic $(\text{Mg}/(\text{Mg}+\text{Fe}))\cdot 100$) of ~90 (Fig. 4d).
272 Some of the orthopyroxene crystals contain clinopyroxene exsolutions. This xenolith also
273 contains veins of SiO_2 - and K_2O -rich silicate melts, typical of the melts produced by low-degree
274 melting of phlogopite-bearing mantle (Condamine and Médard 2014). These melt veins are
275 associated with small (< 100 μm) clinopyroxene crystals with Mg# between 92 and 94. A
276 second and smaller xenolith (DR080205-x1), 2.5 mm long (Fig. 4e), is mostly composed of a
277 single clinopyroxene crystal with orthopyroxene exsolutions, and small included crystals of
278 olivine and orthopyroxene. Mineral compositions are similar to those in the first xenolith. A
279 third investigated xenolith (DR080205-x3), only 2 mm in diameter, is similar to the first one,
280 with mostly olivine and orthopyroxene crystals, and clinopyroxene exsolutions in the

281 orthopyroxene. All xenoliths reacted with the surrounding melts: pyroxene crystals react to
282 form a fine-grained corona of clinopyroxene, olivine, and Ti-magnetite, while olivine crystals
283 are overgrown by an Fo₇₂ olivine rim (Fig. 4d, e).

284 Sample DR080205 also contains a few clinopyroxene megacrysts (Fig. 4f). These
285 megacrysts have a magmatic origin and show an inner, normally zoned core (Mg# 68– 61),
286 surrounded by a more magnesian rim (Mg# 68 – 78). This magnesian rim shows evidence of
287 dissolution and is in turn surrounded by an outer rim made of dendritic clinopyroxene crystals
288 with interstitial glass (Fig. 4f).

289 Quantification of dissolved water has been performed by micro-Raman spectroscopy in
290 melt inclusions hosted by olivine and titanomagnetite crystals. The pre-eruptive water content
291 is constrained to a minimum of 2.3 wt. % for DR01 and 1.2 wt. % for DR08 (Fig. 5). Our
292 preliminary data suggest that open embayments can retain high water contents comparable to
293 those of the closed melt inclusions, suggesting the occurrence of disequilibrium water degassing
294 during magma ascent. Disequilibrium water degassing typically results from fast magma ascent.
295 It can be favored by the low crystal content, and in turn can delay melt crystallization and
296 bubble nucleation (Ferguson et al., 2016; Lloyd et al., 2014).

297

298 **4.2. Thermobarometry**

299 Pre-eruptive temperatures for the main erupted magmas were calculated using the
300 olivine-melt equilibrium and the equations of Beattie (1993) and Ford et al. (1983). Equilibrium
301 olivine-glass pairs were selected based on a Fe/Mg Kd of 0.30 ± 0.05 , assuming a Fe³⁺/Fe_{total}
302 ratio of 0.15, and the temperatures were averaged on 3 – 14 couples per sample. For
303 thermometry calculations, the pressure was arbitrarily set at 200 MPa, however, the influence
304 of pressure is limited to a few degrees per 100 MPa. Results from the model of Beattie (1993),

305 and from the T_{sum} equation of Ford et al. (1983) are within 2 – 8 °C of each other. Anhydrous
306 calculated temperatures were corrected for the effect of H₂O using average H₂O concentration
307 determined by micro-Raman spectrometry and the olivine liquidus depression model of Médard
308 and Grove (2008). Uncorrected pre-eruptive temperatures are 1151 ± 20 °C for phase 1 (DR01-
309 DR10-DR12) and 1136 ± 20 °C for phase 2 (DR08-DR11). Corrected temperatures are within
310 error for all samples, at 1095 ± 20 °C. Note that if melt inclusion provides a minimum pre-
311 eruptive water content, this calculation provides a maximum pre-eruptive temperature.

312 Pre-eruptive temperature and oxygen fugacity for the magma batch parent to the Fo₅₅
313 olivine cores were calculated from an ilmenite-titanomagnetite intergrowth included in Fo₅₅
314 olivine, which constrains magmatic conditions of this evolved batch to 1024 ± 50 °C and an
315 oxygen fugacity (fO₂) close to that of the nickel-nickel oxide buffer (Sauerzapf et al., 2008).
316 Thermometry of melt inclusions in Fo₅₂ olivine gives similar anhydrous temperatures of about
317 1046 ± 20 °C (Beattie, 1993).

318 We analyzed a series of clinopyroxene-orthopyroxene pairs in the mantle xenoliths (Fig.
319 4d, e) to obtain pressure and temperature constraints. In xenolith DR080205-x4, we analyzed
320 clinopyroxene-orthopyroxene pairs associated with the high-SiO₂ high-K₂O veins, as well as
321 exsolutions of clinopyroxene in orthopyroxene. In the other two xenoliths, we only analyzed
322 exsolutions, either of orthopyroxene in clinopyroxene (DR080205-x1), or of clinopyroxene in
323 orthopyroxene (DR080205-x3). Temperatures were calculated using equation (36) of Putirka
324 et al. (2008) with reported uncertainties of 45 °C. For pressure, both equations (38) and (39)
325 were tested against experiments performed at 1.00 GPa by Condamine and Médard (2014) on
326 pyroxene in equilibrium with high-SiO₂ high-K₂O veins. Since equation (38) returned an
327 average pressure of 1.02 GPa, whereas equation (39) returned an average pressure of 0.88,
328 Equation (38) was preferred for the calculation. It reproduces the experimental data with an
329 average error (SEE) of 0.19 GPa. Equilibration pressures for the xenoliths are 0.43 GPa at a

330 temperature of 926 °C for DR080205-x1 (Fig. 6a-c, Suppl. material Table 5), 0.41 GPa at a
331 temperature of 890 °C for DR080205-x3 and 0.46 GPa at a temperature of 913 °C for
332 DR080205-x4. Assuming an average density of 2890 kg m⁻³ for an oceanic crust and 3300 kg
333 m⁻³ for the upper mantle, these xenoliths were equilibrated at an average depth below the sea
334 level of 17 ± 6 km (0.45 ± 0.19 GPa).

335 We made an estimation of the magma storage depth by applying a clinopyroxene- only
336 geobarometer (Equation 32b with water content of 2.3 wt.%, Putirka, 2008) to a zoned
337 clinopyroxene megacryst in sample DR080502-x2 (Fig. 4f). The core of the crystal returns a
338 depth range of 37 to 48 (P = 1.01 – 1.34 GPa). A second cluster with values ranging from 24 to
339 34 (P = 0.62 – 0.92 GPa) is associated with the inner rim. A few low-pressure values (0.14 –
340 0.38 GPa) were obtained on the outer dendritic rim and could indicate crystallization in the
341 conduit during magma ascent (Fig. 6d). Uncertainties associated with these calculations are 10
342 km (0.28 GPa, Putirka 2008). A second analyzed zoned clinopyroxene megacryst generates
343 similar clusters. Phenocrysts in equilibrium with the bulk rock are expected to have Mg# of 75
344 (olivine) and 78 (clinopyroxene), indicating that the most magnesian olivine cores and the
345 clinopyroxene inner rims are in equilibrium with the magma. The more Fe-rich clinopyroxene
346 cores should thus be interpreted as an antecrystic crystal cargo.

347

348 **4.3. Olivine diffusion and residence times**

349 Five different reversely zoned olivine crystals in DR0801-ALF, DR110704 and DR110401
350 samples were investigated (Fig. 7a,b), assuming an initial step function with an olivine core
351 between Fo₅₃₋₆₀ depending on the crystal, surrounded by an overgrowth rim Fo₆₉₋₇₀ (Fig. 7b).
352 Two zoned olivine crystals at the edge of an harzburgite xenolith (DR080502x4) were also

353 modelled, using a step function with a Fo₉₀ olivine core and a Fo₇₂ olivine overgrowth (Fig.
354 7c,d) but without EBSD orientation.

355 The five diffusion profiles in reversely zoned olivine crystals can be modelled with
356 diffusion times of 29 ± 9 , 24 ± 8 , 19 ± 7 , 38 ± 12 and 40 ± 11 days (supplementary material
357 Table 6, errors are given at the two sigma level). Since no EBSD data was acquired in the two
358 normally zoned olivine crystals from xenolith DR080205x4, we can only provide a time bracket
359 using maximum and minimum diffusion coefficient. Thus, these profiles can be modelled with
360 diffusion times between 12 and 69 and between 8 and 47 days. Fits assuming instantaneous
361 growth of the outer rims followed by pure diffusion are excellent with the reversely zoned
362 crystals (supplementary material Table 6), and very good for the xenolith. The assumption of
363 instantaneous crystal growth is supported by the orders of magnitude of difference between
364 crystal growth rates and elemental diffusion rates (e.g., Petrone et al. 2016). These preliminary
365 diffusion times can be interpreted as residence times for the olivine crystals and the xenolith,
366 between injection of the incoming magma in the shallow magma pocket and its eruption at the
367 surface.

368

369 **5. DISCUSSION**

370

371 **5.1. Source**

372

373 The magmas erupted during the ongoing Mayotte eruption are evolved basanite that likely
374 derive from more primitive (unerupted) basanitic mantle melts. The low HREE concentrations
375 and the strongly fractionated REE patterns ($(\text{Tb}/\text{Yb})_{\text{N}} = 2.9 - 3.2$, Fig. 2c) indicate the presence
376 of residual garnet in the mantle source. Moreover, Sm/Yb and La/Sm ratios for the erupted

377 lavas indicate a spinel/garnet lherzolitic source (Fig. 2d). This is consistent with previous
378 studies on subaerial Comoros lavas which suggest that primary magmas are produced by small
379 degrees of partial melting at the depth of the spinel to garnet lherzolite transition, 80 – 100 km
380 (Bachèlery and Hémond, 2016; Class et al., 1998). Furthermore, olivine melilitites in Mayotte
381 volcanic products and evidence of metasomatizing carbonatitic fluids on Grande Comore
382 suggest a CO₂-rich mantle source (Coltorti et al., 1999; Pelleter et al., 2014). The P₂O₅
383 enrichment of the new volcano samples, together with the high Sr and Ba contents, and high
384 Nb/Yb ratio, are consistent with an apatite contribution in the genesis of these lavas. Presence
385 of a mm-sized apatite xenocryst in one of our lava samples suggests a possible assimilation of
386 apatite-bearing veins during the ascent of primary melts formed at a greater depth, as indicated
387 by Pelleter et al., (2014). Homogeneous P₂O₅ enrichment compared to other Comoros lavas is
388 observed in all of our samples (1.6 – 2.0 wt.%, Suppl. material Table 1), which precludes a late
389 assimilation and argues for a mantle source origin of the inferred apatite-bearing veins.

390

391 **5.2. Deep magma reservoir in the lithospheric mantle**

392 The evolved nature (low Mg#, 43 – 47) of the erupted magmas shows that they are not
393 primary products of mantle melting since the expected Mg# of primary mantle melts in
394 equilibrium with Fo₉₀ olivine is ~73, assuming an olivine/melt K_d of 0.30 (Roeder and Emslie,
395 1970). Extensive cooling and crystallization must thus have occurred in a lithospheric magma
396 reservoir (Fig. 8). A back-crystallization model consistent with the general trend of Comoros
397 lavas (Bachèlery and Hémond, 2016; Class et al., 1998; Claude-Ivanaj et al., 1998; Coltorti et
398 al., 1999; Deniel, 1998; Flower, 1973; Nougier et al., 1986; Pelleter et al., 2014; Strong, 1972;
399 Thompson and Flower, 1971) requires approximately 50% crystallization of an olivine-
400 clinopyroxene assemblage (80% clinopyroxene Mg#₉₁₋₇₆ and 20% olivine Fo₉₀₋₇₅) to reproduce

401 the erupted magma compositions (Fig. 2b). This implies that the reservoir, where mantle-
402 derived magma is ponding and differentiating, has a volume of at least $\sim 10 \text{ km}^3$ ($\sim 5 \text{ km}^3$ of
403 erupted magma and the same amount of crystals) and is zoned, with $\sim 5 \text{ km}^3$ of residual dense
404 cumulates. This is a minimum reservoir size, since the estimation relies on the unlikely
405 hypothesis that melt and cumulates were perfectly segregated, and does not take into account
406 any interstitial melt within the cumulates and the contribution of deep CO_2 exsolution. The
407 occurrence of a large reservoir is also supported by ratios of intrusive to extrusive volumes
408 commonly estimated at $\sim 5:1$ for oceanic mid-ocean ridges (Crisp, 1984; White et al., 2006).
409 Since the erupted magma was a true homogeneous liquid, and the few crystals of the main cone-
410 building phase 1 are unzoned, this suggests the system was not disturbed by new primary
411 magma replenishment and was able to evolve to yield a single well-stratified reservoir. In
412 sample DR080205-x2, clinopyroxene megacryst cores were equilibrated at pressures of 1.01 –
413 1.34 GPa (from Putirka, 2008, equation 32b, i.e. 37 – 48 km, Figs 6d and 8). This provides the
414 depth for the main reservoir feeding the current eruption, which is thus located in the
415 lithospheric mantle, in agreement with seismological and geodetic models (Cesca et al., 2020;
416 Lemoine et al., 2020). The slowly waning effusion rate is also characteristic of an eruption fed
417 by a deep reservoir (Wadge, 1981).

418 Magma ascending from lithospheric mantle storage entrained mantle xenoliths from a
419 shallower depth, near the Moho, at an average depth of $17 \pm 6 \text{ km}$. The time between
420 entrainment of the mantle xenoliths and eruption is estimated less than 70 days. Given that the
421 xenoliths were picked up en route to the surface, this is a preliminary estimation of the transfer
422 time between the deep magma reservoir and the eruption site. It is consistent with the 6 weeks
423 of precursory unrest estimated from seismological data (Cesca et al., 2020; Lemoine et al.,
424 2020).

425

5.3. Differentiated shallower magma batch

427 Phase 1 products are crystal-poor lavas with high density of vesicles (Fig. 3b), skeletal
428 crystals (Fig. 4a, b) and high dissolved water content (Fig. 5). Thus, we suggest that during the
429 first year, eruption is fed by direct ascent of magma from the deep reservoir to the surface. The
430 shape and the size of microlites indicate that most micro-crystallization occurred in the shallow
431 part of the ascending dyke. The degree of magmatic evolution increases from phase 1 to phase
432 2 lavas (Fig. 1d). This increase is mirrored by a decrease in vesicularity, vesicle number density
433 (Fig. 3) and dissolved water content (Fig. 5), indicating that late erupted lavas were increasingly
434 outgassed. Reverse zoning in olivine phenocrysts from phase 2 lavas (Fig. 4c) records the
435 interaction between the hot basanitic magma, ascending from the ≥ 37 km deep storage zone,
436 and a second cooler magma batch (Fig. 8). Since transfer times estimated from diffusion in
437 those crystals (~ 1 month) are similar to transfer times estimated from the mantle xenoliths, the
438 zoned olivine crystals probably came from a similar or shallower depth than the xenoliths.
439 Pyroxenes in the mantle xenoliths record a depth of 17 ± 6 km, interpreted to represent the
440 maximum depth of this shallower reservoir (Fig. 6). The inner rim in clinopyroxene megacryst
441 (DR080205-x4, Fig. 4f), equilibrated at pressures of 0.8 ± 0.28 GPa (28 ± 10 km), may indicate
442 the location of a third magma storage zone.

443 Because no seismicity at this shallow depth was detected (ReVoSiMa, 2021), the
444 differentiated magma batch is unlikely to occupy a large dynamic reservoir but rather perhaps
445 magma ponding at the base of the Moho. Analysis of diffusion profiles in reversely zoned
446 olivine from phase 2 lava flows constrain the time between the start of Fo₇₀ olivine
447 crystallization and eruption. We obtain minimum estimations of ~ 1 month for the time between
448 mixing with the shallower magma batch and eruption of the hybrid magma (Fig. 7, Suppl.
449 material Table 6). Magma mixing and transfer of hybrid magma thus occurred during the

450 eruption and were not related to long-term precursor activity detected by the permanent land-
451 based monitoring networks.

452

453 **5.4. Eruption trigger**

454 The erupted products are evolved alkaline mafic magmas and have a minimum
455 dissolved water content of ca. 2 wt. % (Fig. 5). Available thermodynamic models permit us to
456 crudely estimate the pre-eruptive dissolved CO₂ content as being in the range 0.6 – 1.2 wt %
457 (Allison et al., 2019; Papale et al., 2006). This is compatible with the possible presence of an
458 exsolved CO₂-rich fluid phase in the plumbing system. Under these conditions, the magma
459 chamber will be pressurized, but stable. Because of the deep location and the associated
460 pressure, volume changes due to crystallization or volatile exsolution should not be sufficient
461 to act as an eruption trigger. Moreover, we found no evidence of primitive magma in the erupted
462 products. Therefore, we suggest that fault movement or earthquakes rather than a deep reservoir
463 recharge event was responsible for the sudden initial decompression and fast ascent of a large
464 volume of volatile-rich melt stored in the mantle.

465 The eruption site belongs to a WNW-ESE volcano-tectonic ridge, parallel to regional
466 trends, suggesting relation to a pre-existing tectonic structure. Deep seismicity recorded during
467 the seismo-volcanic crisis (Cesca et al., 2020; Lemoine et al., 2020; ReVoSiMa, 2021) implies
468 that these structures are deeply rooted in the lithosphere (up to 50 km depth). The sequence of
469 strong tectonic earthquakes recorded at the beginning of the eruption (volcano-tectonic events
470 located at 34 – 41 km depth, 35 km east of Mayotte (Cesca et al., 2020; Lemoine et al., 2020)
471 might thus be related to the movement along the lithospheric faults.

472

473 5.5. Syn-eruptive magma path change

474 Since the melt was volatile-saturated ($\text{CO}_2+\text{H}_2\text{O}$) in the deep reservoir, magma ascent
475 towards the surface would have resulted in continuous exsolution of CO_2 first and then
476 $\text{CO}_2+\text{H}_2\text{O}$ up to the eruption site. Full exsolution of pre-eruptive dissolved volatiles at the vent
477 would produce a fluid with a molar volume of ca. $320 \text{ cm}^3/\text{mol}$ and vesicularity in the range 54
478 – 71 vol%, values much higher than those measured in our samples (Suppl. material Tables 2
479 and 3). Vesicularity would be even higher if there were additional exsolved CO_2 in the reservoir.
480 Incomplete disequilibrium degassing because of the fast ascent rate and rapid quenching on the
481 seafloor can explain the difference between the expected and measured vesicularities. We also
482 suggest that rapid decompression-induced crystallization (Hammer et al., 1999) in the shallow
483 conduit may be responsible for the skeletal shape of olivine and Ti-magnetite crystals (Faure et
484 al., 2003). The absence of reversely zoned olivine crystals in phase 1 products suggests that
485 basaltic melts ascended from the deep reservoir directly to the surface during the first year of
486 eruption (Fig. 8).

487 In contrast, the presence of reversely zoned olivine with Fo_{53} cores in phase 2 lava flows
488 (Fig. 4c) indicates that, after May 2019 magma ascending from the deep reservoir intersected a
489 more evolved magma batch, at a depth near the Moho on its way to the surface (Fig. 8). Using
490 a simple mass balance model, we estimate that only 6% of the evolved magma (represented by
491 melt inclusions in Fo_{53} olivine in sample DR11) was assimilated in the erupted lavas, indicating
492 that the intersected volume of this shallower reservoir is much smaller than the deeper one. Less
493 abundant (low N_v) and larger vesicles (Fig. 3) are consistent with a slower ascent and lower
494 volatile content during phase 2. The residual magmatic liquid in the shallower magma batch
495 could have been produced by fractional crystallization from an older magma intrusion, as
496 observed during Kilauea's 2018 eruption (Gansecki et al., 2019). Due to the time required for
497 magmatic differentiation (decades, Gansecki et al., 2019), this observation implies magma

498 intrusion and possible recent volcanic activity in the offshore part of the volcanic ridge prior to
499 the current eruption. The emission of the more evolved magma in phase 2 could have resulted
500 either from a change in the dyke pathway (as suggested by the presence of mantle xenoliths)
501 and/or a decrease in magma discharge rate allowing the input from the second shallower magma
502 source.

503 Zoned olivine phenocrysts took ~ 1 month to be transferred from the ~ 17 km shallow
504 reservoir to the seafloor. Thus, we obtain a minimum ascent rate of 0.005 m.s^{-1} from the shallow
505 reservoir to the surface for the slower pathway (Fig. 8).

506

507 **6. CONCLUSIONS**

508 The large and long-lasting effusive eruption offshore from Mayotte is fed by a deep ($>$
509 37 km) and large ($\geq 10 \text{ km}^3$) pre-existing mantle reservoir of evolved, alkaline magma that
510 experienced extensive crystallization. This has important volcanic hazard implications, because
511 it demonstrates that this large, volatile-rich deep reservoir could quickly be tapped in a
512 tectonically active region to feed a voluminous and long-lasting effusive eruption. During the
513 eruption, magma ascent slowed and switched to a pathway that sampled a small more
514 chemically evolved shallower magma batch at the base of the crust. Our petrological study
515 provides important constraints on the entire deep magmatic system from the source to the
516 surface. These results bring valuable and critical information complementary to geophysical
517 datasets, showing that we can use the petrology of erupted products for long-term monitoring
518 of extreme events even when they occur in poorly accessible environments. These data helped
519 to determine the geometry and the dynamics of magmatic plumbing systems, and provided
520 critical constraints for the interpretation of geophysical datasets in terms of processes and
521 patterns.

522

523 **Acknowledgements**

524 MAYOBS 1 campaign was funded by the CNRS-INSU TELLUS MAYOTTE program
525 (SISMAYOTTE project). MAYOBS 1, 2 and 4 campaigns were conducted by several French
526 research institutions and laboratories (IPGP/CNRS/BRGM/IFREMER/IPGS). We want to
527 thank the crew of R/V Marion Dufresne (TAAF/IFREMER/LDA). Analyses were funded by
528 the Service National d'Observation en Volcanologie (SNOV, INSU) and the Réseau de
529 Surveillance Volcanologique et Sismologique de Mayotte (REVOSIMA), a partnership
530 between the Institut de Physique du Globe de Paris (IPGP), the Bureau de Recherches
531 Géologiques et Minières (BRGM), and the Observatoire Volcanologique du Piton de la
532 Fournaise (OVPF-IPGP), the Centre National de la Recherche Scientifique (CNRS), and the
533 Institut Français de Recherche pour l'Exploitation de la Mer (IFREMER). The authors would
534 like to thank Andrew Harris for reviewing and English improvement before submission,
535 IFREMER for their welcome during the sampling and E. Humler for his support and national
536 funding coordination (CNRS, REVOSIMA). Raman data were acquired by ADM as a side
537 project during his fellowship at the Center for Advanced Studies of the Ludwig-Maximilians-
538 Universität München (CAS LMU) in collaboration with the CAS Research Group on "Magma
539 to Tephra: Ash in the Earth System" (Resp. Prof. Donald Dingwell). We thank Ivonne Cocca
540 (Université de Paris) for assistance in sample preparation. Finally, we are also grateful for the
541 helpful reviews provided by William Chadwick, an anonymous reviewer, and editorial handling
542 by Chiara Petrone. This is a Labex ClerVolc contribution number 466.

543 **References**

544 Allison, C.M., Roggensack, K., Clarke, A.B., 2019. H₂O–CO₂ solubility in alkali-rich mafic
545 magmas: new experiments at mid-crustal pressures. *Contrib. Mineral. Petrol.* 174, 58.
546 <https://doi.org/10.1007/s00410-019-1592-4>

- 547 Bachèlery, P., Hémond, C., 2016. Geochemical and Petrological Aspects of Karthala Volcano,
548 in: *Active Volcanoes of the Southwest Indian Ocean*. Springer, pp. 367–384.
- 549 Bachèlery, P., Morin, J., Villeneuve, N., Soulé, H., Nassor, H., Ali, A.R., 2016. Structure and
550 eruptive history of Karthala volcano, in: *Active Volcanoes of the Southwest Indian Ocean*.
551 Springer, pp. 345–366.
- 552 Beattie, P., 1993. Olivine-melt and orthopyroxene-melt equilibria. *Contrib. Mineral. Petrol.*
553 115, 103–111. <https://doi.org/10.1007/BF00712982>
- 554 Bottinga, Y., Weill, D.F., 1970. Densities of liquid silicate systems calculated from partial
555 molar volumes of oxide components. *Am. J. Sci.* 269, 169–182.
- 556 Carey, R., Soule, S.A., Manga, M., White, J.D.L., McPhie, J., Wysoczanski, R., Jutzeler, M.,
557 Tani, K., Yoerger, D., Fornari, D., 2018. The largest deep-ocean silicic volcanic eruption
558 of the past century. *Sci. Adv.* 4, e1701121. <https://doi.org/10.1126/sciadv.1701121>
- 559 Cesca, S., Letort, J., Razafindrakoto, H.N.T., Heimann, S., Rivalta, E., Isken, M.P., Nikkhoo,
560 M., Passarelli, L., Petersen, G.M., Cotton, F., Dahm, T., 2020. Drainage of a deep magma
561 reservoir near Mayotte inferred from seismicity and deformation. *Nat. Geosci.* 13, 87–93.
562 <https://doi.org/10.1038/s41561-019-0505-5>
- 563 Chadwick, W.W., Merle, S.G., Baker, E.T., Walker, S.L., Resing, J.A., Butterfield, D.A.,
564 Anderson, M.O., Baumberger, T., Bobbitt, A.M., 2018. A recent volcanic eruption
565 discovered on the central Mariana back-arc spreading center. *Front. Earth Sci.* 6, 172.
566 <https://doi.org/10.3389/feart.2018.00172>
- 567 Chadwick, W.W., Paduan, J.B., Clague, D.A., Dreyer, B.M., Merle, S.G., Bobbitt, A.M.,
568 Caress, D.W., Philip, B.T., Kelley, D.S., Nooner, S.L., 2016. Voluminous eruption from
569 a zoned magma body after an increase in supply rate at Axial Seamount. *Geophys. Res.*
570 *Lett.* 43, 12063–12070. <https://doi.org/10.1002/2016GL071327>.
- 571 Chavrit, D., Humler, E., Grasset, O., 2014. Mapping modern CO₂ fluxes and mantle carbon
572 content all along the mid-ocean ridge system. *Earth Planet. Sci. Lett.* 387, 229–239.
573 <https://doi.org/10.1016/j.epsl.2013.11.036>
- 574 Chavrit, D., Humler, E., Morizet, Y., Laporte, D., 2012. Influence of magma ascent rate on
575 carbon dioxide degassing at oceanic ridges: Message in a bubble. *Earth Planet. Sci. Lett.*
576 357, 376–385. <https://doi.org/10.1016/j.epsl.2012.09.042>
- 577 Clague, D.A., Paduan, J.B., Caress, D.W., Thomas, H., Chadwick Jr, W.W., Merle, S.G., 2011.
578 Volcanic morphology of West Mata Volcano, NE Lau Basin, based on high-resolution
579 bathymetry and depth changes. *Geochemistry, Geophys. Geosystems* 12.
580 <https://doi.org/10.1029/2011GC003791>
- 581 Clague, D.A., Paduan, J.B., Dreyer, B.M., Chadwick Jr, W.W., Rubin, K.R., Perfit, M.R.,
582 Fundis, A.T., 2018. Chemical variations in the 1998, 2011, and 2015 lava flows from Axial
583 Seamount, Juan de Fuca Ridge: Cooling during ascent, lateral transport, and flow.
584 *Geochemistry, Geophys. Geosystems* 19, 2915–2933.
585 <https://doi.org/10.1029/2018GC007708>
- 586 Class, C., Goldstein, S.L., Altherr, R., Bachèlery, P., 1998. The process of plume–lithosphere
587 interactions in the ocean basins—the case of Grande Comore. *J. Petrol.* 39, 881–903.
588 <https://doi.org/10.1093/etroj/39.5.881>

- 589 Class, C., Goldstein, S.L., Shirey, S.B., 2009. Osmium isotopes in Grande Comore lavas: a new
590 extreme among a spectrum of EM-type mantle endmembers. *Earth Planet. Sci. Lett.* 284,
591 219–227. <https://doi.org/10.1016/j.epsl.2009.04.031>
- 592 Class, C., Goldstein, S.L., Stute, M., Kurz, M.D., Schlosser, P., 2005. Grand Comore Island: A
593 well-constrained “low $^3\text{He}/^4\text{He}$ ” mantle plume. *Earth Planet. Sci. Lett.* 233, 391–409.
594 <https://doi.org/10.1016/j.epsl.2005.02.029>
- 595 Claude-Ivanaj, C., Bourdon, B., Allègre, C.J., 1998. Ra–Th–Sr isotope systematics in Grande
596 Comore Island: a case study of plume–lithosphere interaction. *Earth Planet. Sci. Lett.* 164,
597 99–117. [https://doi.org/10.1016/S0012-821X\(98\)00195-2](https://doi.org/10.1016/S0012-821X(98)00195-2)
- 598 Coltorti, M., Bonadiman, C., Hinton, R.W., Siena, F., Upton, B.G.J., 1999. Carbonatite
599 metasomatism of the oceanic upper mantle: evidence from clinopyroxenes and glasses in
600 ultramafic xenoliths of Grande Comore, Indian Ocean. *J. Petrol.* 40, 133–165.
601 <https://doi.org/10.1016/j.epsl.2014.04.027>
- 602 Condamine, P., Médard, E., 2014. Experimental melting of phlogopite-bearing mantle at 1 GPa:
603 Implications for potassic magmatism. *Earth Planet. Sci. Lett.* 397, 80–92.
604 <https://doi.org/10.1016/j.epsl.2014.04.027>
- 605 Crisp, J.A., 1984. Rates of magma emplacement and volcanic output. *J. Volcanol. Geotherm.*
606 *Res.* 20, 177–211. [https://doi.org/10.1016/0377-0273\(84\)90039-8](https://doi.org/10.1016/0377-0273(84)90039-8)
- 607 Costa, F., Dohmen, R., Chakraborty, S., 2008. Time scales of magmatic processes from
608 modeling the zoning patterns of crystals. *Rev. Mineral. Geochemistry* 69, 545–594.
609 <https://doi.org/10.2138/rmg.2008.69.14>
- 610 Couperthwaite, F.K., Morgan, D.J., Pankhurst, M.J., Lee, P.D., Day, J.M.D., 2021. Reducing
611 epistemic and model uncertainty in ionic inter-diffusion chronology: A 3D observation
612 and dynamic modeling approach using olivine from Piton de la Fournaise, La Réunion.
613 *Am. Mineral. J. Earth Planet. Mater.* 106, 481–494. <https://doi.org/10.2138/am-2021-7296CCBY>
- 615 Debeuf, D., 2004. Étude de l'évolution volcano-structurale et magmatique de Mayotte (archipel
616 des Comores, océan Indien). PhD thesis, Université de la Réunion, France.
- 617 Deniel, C., 1998. Geochemical and isotopic (Sr, Nd, Pb) evidence for plume–lithosphere
618 interactions in the genesis of Grande Comore magmas (Indian Ocean). *Chem. Geol.* 144,
619 281–303. [https://doi.org/10.1016/S0009-2541\(97\)00139-3](https://doi.org/10.1016/S0009-2541(97)00139-3)
- 620 Di Muro, A., Métrich, N., Vergani, D., Rosi, M., Armienti, P., Fougeroux, T., Deloule, E.,
621 Arienzo, I., Civetta, L., 2014. The shallow plumbing system of Piton de la Fournaise
622 Volcano (La Reunion Island, Indian Ocean) revealed by the major 2007 caldera-forming
623 eruption. *J. Petrol.* 55, 1287–1315. <https://doi.org/10.1093/petrology/egu025>
- 624 Di Muro, A., Villemant, B., Montagnac, G., Scaillet, B., Reynard, B., 2006. Quantification of
625 water content and speciation in natural silicic glasses (phonolite, dacite, rhyolite) by
626 confocal microRaman spectrometry. *Geochim. Cosmochim. Acta* 70, 2868–2884.
627 <https://doi.org/10.1016/j.gca.2006.02.016>
- 628 Dofal, A., Fontaine, F.R., Michon, L., Barruol, G., Tkalcic, H., 2018. Crustal structure variation
629 across the southwestern Indian Ocean from receiver functions determined at Ocean-
630 Bottom Seismometers, in: AGU Fall Meeting 2018. AGU.

- 631 Edmonds, M., Sides, I.R., Swanson, D.A., Werner, C., Martin, R.S., Mather, T.A., Herd, R.A.,
632 Jones, R.L., Mead, M.I., Sawyer, G., 2013. Magma storage, transport and degassing during
633 the 2008–10 summit eruption at Kīlauea Volcano, Hawai‘i. *Geochim. Cosmochim. Acta*
634 123, 284–301. <https://doi.org/10.1016/j.gca.2013.05.038>
- 635 Emerick, C.M., Duncan, R.A., 1982. Age progressive volcanism in the Comores Archipelago,
636 western Indian Ocean and implications for Somali plate tectonics. *Earth Planet. Sci. Lett.*
637 60, 415–428. [https://doi.org/10.1016/0012-821X\(82\)90077-2](https://doi.org/10.1016/0012-821X(82)90077-2)
- 638 Famin, V., Michon, L., Bourhane, A., 2020. The Comoros archipelago: a right-lateral transform
639 boundary between the Somalia and Lwandle plates. *Tectonophysics* 789, 228539.
640 <https://doi.org/10.1016/j.tecto.2020.228539>
- 641 Faure, F., Trolliard, G., Nicollet, C., Montel, J.-M., 2003. A developmental model of olivine
642 morphology as a function of the cooling rate and the degree of undercooling. *Contrib.*
643 *Mineral. Petrol.* 145, 251–263. <https://doi.org/10.1007/s00410-003-0449-y>
- 644 Ferguson, D.J., Gonnermann, H.M., Ruprecht, P., Plank, T., Hauri, E.H., Houghton, B.F.,
645 Swanson, D.A., 2016. Magma decompression rates during explosive eruptions of Kīlauea
646 volcano, Hawaii, recorded by melt embayments. *Bull. Volcanol.* 78, 71.
647 <https://doi.org/10.1007/s00445-016-1064-x>
- 648 Feuillet, N., 2019. MAYOBS1 cruise, RV Marion Dufresne.
649 <https://doi.org/10.17600/18001217>
- 650 Feuillet, N., Jorry, S., Rinnert, E., Thinon, I., Fouquet, Y., 2019. MAYOBS cruises, RV Marion
651 Dufresne. <https://doi.org/10.18142/291>
- 652 Feuillet, N., Jorry, S.J., Crawford, W., Deplus, C., Thinon, I., Jacques, E., Saurel, J.M.,
653 Lemoine, A., Paquet, F., Satriano, C., Aiken, C., Foix, O., Kowalski, P., Laurent, A.,
654 Rinnert, E., Cathalot, C., Donval, J.P., Guyader, V., Gaillot, A., Scalabrin, C., Moreira,
655 M., Peltier, A., Beauducel, F., Grandin, R., Ballu, V., Daniel, R., Pelleau, P., Gomez, J.,
656 Besançon, S., Geli, L., Bernard, P., Bachelery, P., Fouquet, Y., Bertil, D., Lemarchand,
657 A., van der Woerd, J., 2020. Birth of a large volcanic edifice through lithosphere-scale
658 diking offshore Mayotte (Indian Ocean). *EarthArXiv*. <https://doi.org/10.31223/X5B89P>
- 659 Flower, M.F.J., 1973. Evolution of basaltic and differentiated lavas from Anjouan, Comores
660 Archipelago. *Contrib. to Mineral. Petrol.* 38, 237–260.
- 661 Ford, C.E., Russell, D.G., Craven, J.A., Fisk, M.R., 1983. Olivine-liquid equilibria:
662 temperature, pressure and composition dependence of the crystal/liquid cation partition
663 coefficients for Mg, Fe²⁺, Ca and Mn. *J. Petrol.* 24, 256–266.
664 <https://doi.org/10.1093/petrology/24.3.256>
- 665 Fouquet, Y., Feuillet, N., 2019. MAYOBS4 cruise, RV Marion Dufresne.
666 <https://doi.org/10.17600/18001238>
- 667 Gansecki, C., Lee, R.L., Shea, T., Lundblad, S.P., Hon, K., Parcheta, C., 2019. The tangled tale
668 of Kīlauea’s 2018 eruption as told by geochemical monitoring. *Science* (80-.). 366.
669 <https://doi.org/10.1126/science.aaz0147>
- 670 Girona, T., Costa, F., 2013. DIPRA: A user-friendly program to model multi-element diffusion
671 in olivine with applications to timescales of magmatic processes. *Geochemistry, Geophys.*
672 *Geosystems* 14, 422–431. <https://doi.org/10.1029/2012GC004427>

- 673 Gurioli, L., Di Muro, A., Vlastélic, I., Moune, S., Thivet, S., Valer, M., Villeneuve, N.,
674 Boudoire, G., Peltier, A., Bachèlery, P., 2018. Integrating field, textural, and geochemical
675 monitoring to track eruption triggers and dynamics: a case study from Piton de la
676 Fournaise. *Solid Earth* 9, 431–455. <https://doi.org/10.5194/se-9-431-2018>
- 677 Hajash, A., Armstrong, R.L., 1972. Paleomagnetic and radiometric evidence for the age of the
678 Comores Islands, west central Indian Ocean. *Earth Planet. Sci. Lett.* 16, 231–236.
679 [https://doi.org/10.1016/0012-821X\(72\)90195-1](https://doi.org/10.1016/0012-821X(72)90195-1)
- 680 Hammer, J.E., Cashman, K. V, Hoblitt, R.P., Newman, S., 1999. Degassing and microlite
681 crystallization during pre-climactic events of the 1991 eruption of Mt. Pinatubo,
682 Philippines. *Bull. Volcanol.* 60, 355–380. <https://doi.org/10.1007/s004450050238>
- 683 Hart, S.R., Davis, K.E., 1978. Nickel partitioning between olivine and silicate melt. *Earth*
684 *Planet. Sci. Lett.* 40, 203–219.
- 685 Hassen Ali, T., 2020. Etude pétrochimique du volcanisme récent de Mayotte. Master thesis,
686 Université Clermont Auvergne, Clermont-Ferrand, France.
- 687 Houghton, B.F., Wilson, C.J.N., 1989. A vesicularity index for pyroclastic deposits. *Bull.*
688 *Volcanol.* 51, 451–462. <https://doi.org/10.1007/BF01078811>
- 689 Jorry, S.J., 2019. MAYOBS2 cruise, RV Marion Dufresne. <https://doi.org/10.17600/18001222>
- 690 Lemoine, A., Briole, P., Bertil, D., Roullé, A., Foumel, M., THINON, I., Raucoules, D.,
691 Michele, M. de, Valty, P., 2020. The 2018-2019 seismo-volcanic crisis east of Mayotte,
692 Comoros islands: seismicity and ground deformation markers of an exceptional submarine
693 eruption. *Geophys. J. International* 223(1): 22-44. <https://doi.org/10.31223/osf.io/d46xj>
- 694 Lloyd, A.S., Ruprecht, P., Hauri, E.H., Rose, W., Gonnermann, H.M., Plank, T., 2014.
695 NanoSIMS results from olivine-hosted melt embayments: magma ascent rate during
696 explosive basaltic eruptions. *J. Volcanol. Geotherm. Res.* 283, 1–18.
697 <https://doi.org/10.1016/j.jvolgeores.2014.06.002>
- 698 Médard, E., Grove, T.L., 2008. The effect of H₂O on the olivine liquidus of basaltic melts:
699 experiments and thermodynamic models. *Contrib. Mineral. Petrol.* 155, 417–432.
700 <https://doi.org/10.1007/s00410-007-0250-4>
- 701 Michon, L., 2016. The volcanism of the Comoros archipelago integrated at a regional scale, in:
702 *Active Volcanoes of the Southwest Indian Ocean*. Springer, pp. 333–344.
703 https://doi.org/10.1007/978-3-642-31395-0_21
- 704 Nehlig, P., Lacquement, F., Bernard, J., Caroff, M., Deparis, J., Jaouen, T., Pelleter, A.A.,
705 Perrin, J., Prognon, C., Vittecoq, B., 2013. Notice de la carte géologique de Mayotte.
706 BRGM/RP-61803-FR, 135 p., 45 ill., 1 ann.
- 707 Nougier, J., Cantagrel, J.M., Karche, J.P., 1986. The Comores archipelago in the western Indian
708 Ocean: volcanology, geochronology and geodynamic setting. *J. African Earth Sci.* 5, 135–
709 144. [https://doi.org/10.1016/0899-5362\(86\)90003-5](https://doi.org/10.1016/0899-5362(86)90003-5)
- 710 Oppenheimer, C., Orchard, A., Stoffel, M., Newfield, T.P., Guillet, S., Corona, C., Sigl, M., Di
711 Cosmo, N., Büntgen, U., 2018. The Eldgjá eruption: timing, long-range impacts and
712 influence on the Christianisation of Iceland. *Clim. Change* 147, 369–381.
713 <https://doi.org/10.1007/s10584-018-2171-9>

- 714 Papale, P., Moretti, R., Barbato, D., 2006. The compositional dependence of the saturation
715 surface of H₂O+ CO₂ fluids in silicate melts. *Chem. Geol.* 229, 78–95.
716 <https://doi.org/10.1016/j.chemgeo.2006.01.013>
- 717 Patrick, M., Johanson, I., Shea, T., Waite, G., 2020. The historic events at Kīlauea Volcano in
718 2018: summit collapse, rift zone eruption, and Mw 6.9 earthquake: preface to the special
719 issue. *Bull. Volcanol.* 82, 46. <https://doi.org/0.1007/s00445-020-01377-5>
- 720 Pelleter, A.-A., Caroff, M., Cordier, C., Bachèlery, P., Nehlig, P., Debeuf, D., Arnaud, N., 2014.
721 Melilite-bearing lavas in Mayotte (France): An insight into the mantle source below the
722 Comores. *Lithos* 208, 281–297. <https://doi.org/10.1016/j.lithos.2014.09.012>
- 723 Perfit, M.R., Chadwick, W.W., 1998. Magmatism at mid-ocean ridges: Constraints from
724 volcanological and geochemical investigations. *Geophys. Monogr. Geophys. Union* 106,
725 59–116.
- 726 Petrone, C.M., Bugatti, G., Braschi, E., Tommasini, S., 2016. Pre-eruptive magmatic processes
727 re-timed using a non-isothermal approach to magma chamber dynamics. *Nat. Commun.* 7,
728 1–11. <https://doi.org/10.1038/ncomms12946>
- 729 Pouclet, A., Bellon, H., Bram, K., 2016. The Cenozoic volcanism in the Kivu rift: Assessment
730 of the tectonic setting, geochemistry, and geochronology of the volcanic activity in the
731 South-Kivu and Virunga regions. *J. African Earth Sci.* 121, 219–246.
732 <https://doi.org/10.1016/j.jafrearsci.2016.05.026>
- 733 Putirka, K.D., 2008. Thermometers and Barometers for Volcanic Systems. *Rev. Mineral.*
734 *Geochemistry* 69, 61–120. <https://doi.org/10.2138/rmg.2008.69.3>
- 735 Resing, J.A., Rubin, K.H., Embley, R.W., Lupton, J.E., Baker, E.T., Dziak, R.P., Baumberger,
736 T., Lilley, M.D., Huber, J.A., Shank, T.M., 2011. Active submarine eruption of boninite
737 in the northeastern Lau Basin. *Nat. Geosci.* 4, 799–806. <https://doi.org/10.1038/ngeo1275>
- 738 ReVoSiMa, 2021. Bulletin n°21 de l'activité sismo-volcanique à Mayotte, du 1 au 31 janvier
739 2021. ISSN : 2680-1205. [https://www.brgm.fr/sites/default/files/documents/2021-
740 02/dossier-thematique-mayotte-bulletin-revosima-026.pdf](https://www.brgm.fr/sites/default/files/documents/2021-02/dossier-thematique-mayotte-bulletin-revosima-026.pdf)
- 741 Roeder, P.L., Emslie, Rf., 1970. Olivine-liquid equilibrium. *Contrib. to Mineral. Petrol.* 29,
742 275–289.
- 743 Rubin, K.H., Soule, S.A., Chadwick, W.W., Fornari, D.J., Clague, D.A., Embley, R.W., Baker,
744 E.T., Perfit, M.R., Caress, D.W., Dziak, R.P., 2012. Volcanic eruptions in the deep sea.
745 *Oceanography* 25, 142–157.
- 746 Saria, E., Calais, E., Stamps, D.S., Delvaux, D., Hartnady, C.J.H., 2014. Present-day kinematics
747 of the East African Rift. *J. Geophys. Res. Solid Earth* 119, 3584–3600.
748 <https://doi.org/10.1002/2013JB010901>
- 749 Sauerzapf, U., Lattard, D., Burchard, M., Engelmann, R., 2008. The Titanomagnetite - Ilmenite
750 Equilibrium: New Experimental Data and Thermo-oxybarometric Application to the
751 Crystallization of Basic to Intermediate Rocks. *J. Petrol.* 49, 1161–1185.
752 <https://doi.org/10.1093/petrology/egn021>
- 753 Shea, T., Houghton, B.F., Gurioli, L., Cashman, K. V, Hammer, J.E., Hobden, B.J., 2010.
754 Textural studies of vesicles in volcanic rocks: an integrated methodology. *J. Volcanol.*

- 755 Geotherm. Res. 190, 271–289. <https://doi.org/10.1016/j.jvolgeores.2009.12.003>
- 756 Späth, A., Roex, A.P. Le, Duncan, R.A., 1996. The geochemistry of lavas from the Comores
757 Archipelago, Western Indian Ocean: petrogenesis and mantle source region
758 characteristics. *J. Petrol.* 37, 961–991. <https://doi.org/10.1093/petrology/37.4.961>
- 759 Stamps, D.S., Saria, E., Kreemer, C., 2018. A Geodetic Strain Rate Model for the East African
760 Rift System. *Sci. Rep.* 8, 732. <https://doi.org/10.1038/s41598-017-19097-w>
- 761 Strong, D.F., 1972. Petrology of the island of Moheli, western Indian Ocean. *Geol. Soc. Am.*
762 *Bull.* 83, 389–406.
- 763 Thivet, S., Gurioli, L., Di Muro, A., 2020. Basaltic dyke eruptions at Piton de La Fournaise:
764 characterization of the eruptive products with implications for reservoir conditions,
765 conduit processes and eruptive dynamics. *Contrib. to Mineral. Petrol.* 175, 1–24.
766 <https://doi.org/10.1007/s00410-020-1664-5>
- 767 Thompson, R.N., Flower, M.F.J., 1971. One-atmosphere melting and crystallization relations
768 of lavas from Anjouan, Comores Archipelago, Western Indian Ocean. *Earth Planet. Sci.*
769 *Lett.* 12, 97–107. [https://doi.org/10.1016/0012-821X\(71\)90060-4](https://doi.org/10.1016/0012-821X(71)90060-4)
- 770 Thordarson, T., Miller, D.J., Larsen, G., Self, S., Sigurdsson, H., 2001. New estimates of sulfur
771 degassing and atmospheric mass-loading by the 934 AD Eldgjá eruption, Iceland. *J.*
772 *Volcanol. Geotherm. Res.* 108, 33–54. [https://doi.org/10.1016/S0377-0273\(00\)00277-8](https://doi.org/10.1016/S0377-0273(00)00277-8)
- 773 Thordarson, T., Self, S., 1993. The Laki (Skaftár Fires) and Grímsvötn eruptions in 1783–1785.
774 *Bull. Volcanol.* 55, 233–263. <https://doi.org/10.1007/BF00624353>
- 775 Tzevahirtzian, A., Zaragosi, S., Bachèlery, P., Biscara, L., Marchès, E., 2020. Submarine
776 morphology of the Comoros volcanic archipelago. *Mar. Geol.* 432.
777 <https://doi.org/10.1016/j.margeo.2020.106383>
- 778 Wadge, G., 1981. The variation of magma discharge during basaltic eruptions. *J. Volcanol.*
779 *Geotherm. Res.* 11, 139–168. [https://doi.org/10.1016/0377-0273\(81\)90020-2](https://doi.org/10.1016/0377-0273(81)90020-2)
- 780 White, S.M., Crisp, J.A., Spera, F.J., 2006. Long-term volumetric eruption rates and magma
781 budgets. *Geochemistry, Geophys. Geosystems* 7. <https://doi.org/10.1029/2005GC001002>
- 782 Zinke, J., Reijmer, J.J.G., Thomassin, B.A., Dullo, W.-C., Grootes, P.M., Erlenkeuser, H.,
783 2003. Postglacial flooding history of Mayotte lagoon (Comoro archipelago, southwest
784 Indian Ocean). *Mar. Geol.* 194, 181–196. [https://doi.org/10.1016/S0025-3227\(02\)00705-](https://doi.org/10.1016/S0025-3227(02)00705-3)
785 3

786

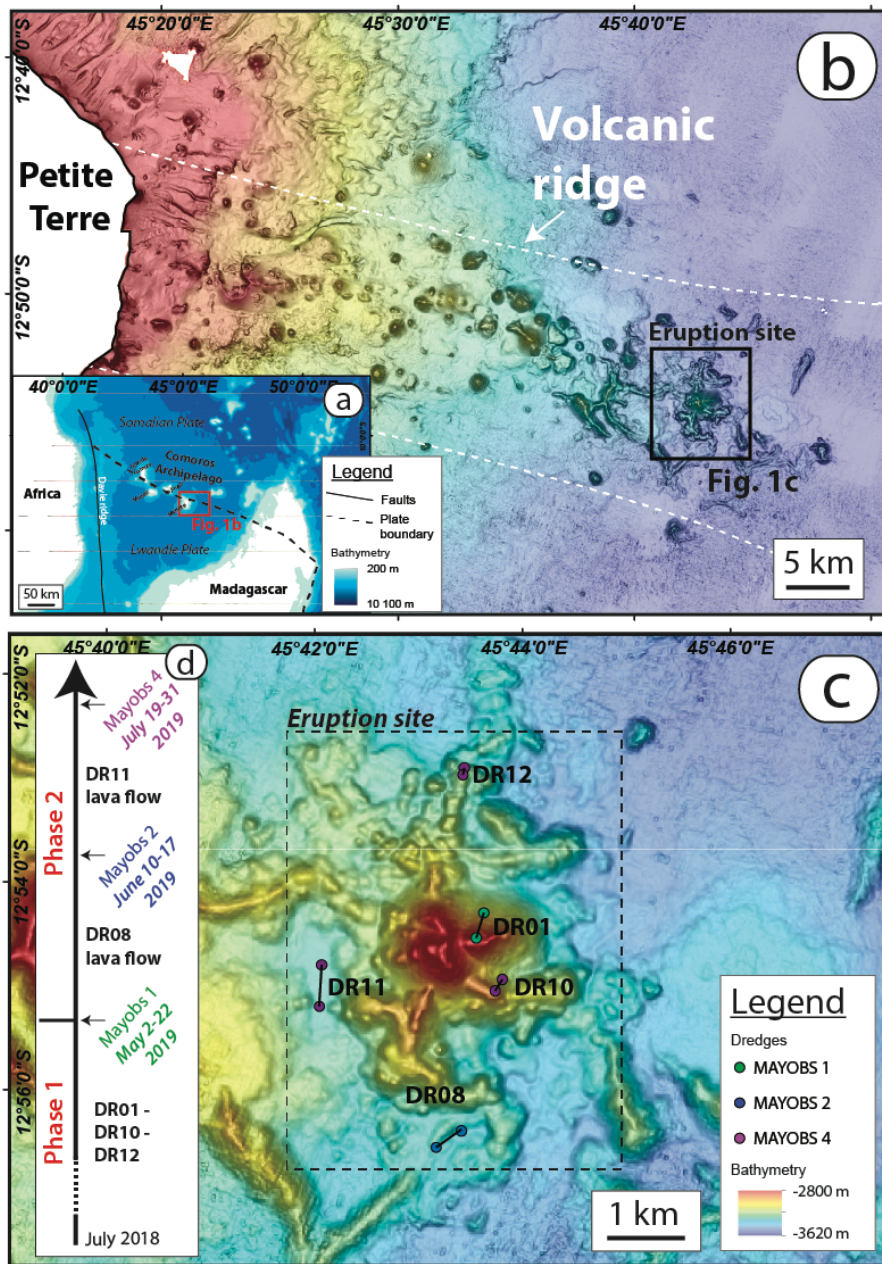
787

788

789

790

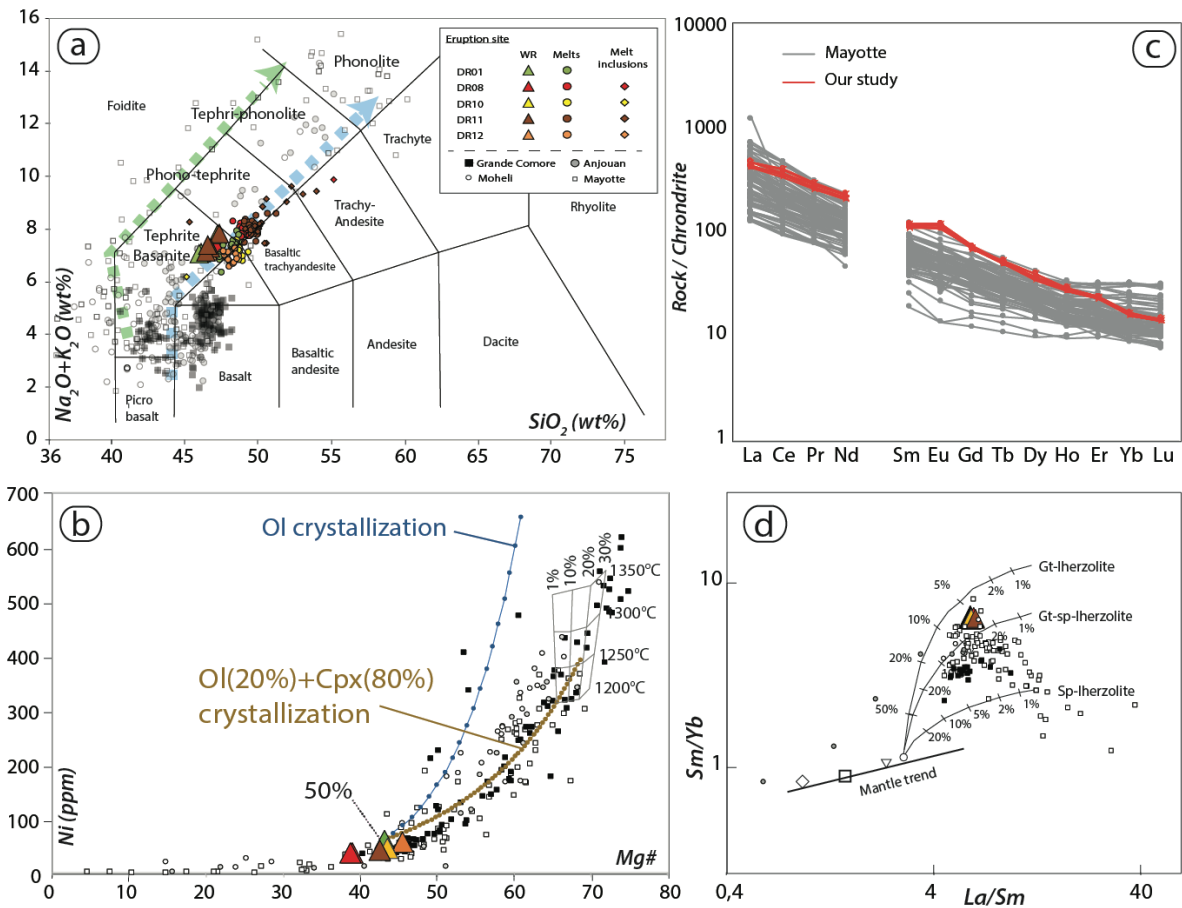
791



793

794 **Fig. 1:** Location of the eruptive site. a) Comoros volcanic archipelago is located in the northern
 795 part of the Mozambique Channel. b) Location of the new volcanic edifice 50 km east of Mayotte
 796 along the submarine volcanic ridge crossing Mayotte eastern flank. c) Location of the five
 797 dredges (DR) carried out during the three oceanographic campaigns (MAYOBS 1, 2 and 4),
 798 superimposed on bathymetric data from the MAYOBS 1 cruise (May 2019). d) Sampling
 799 related to eruption timing. DR01, DR10 and DR12 lavas were erupted before May 2019 during

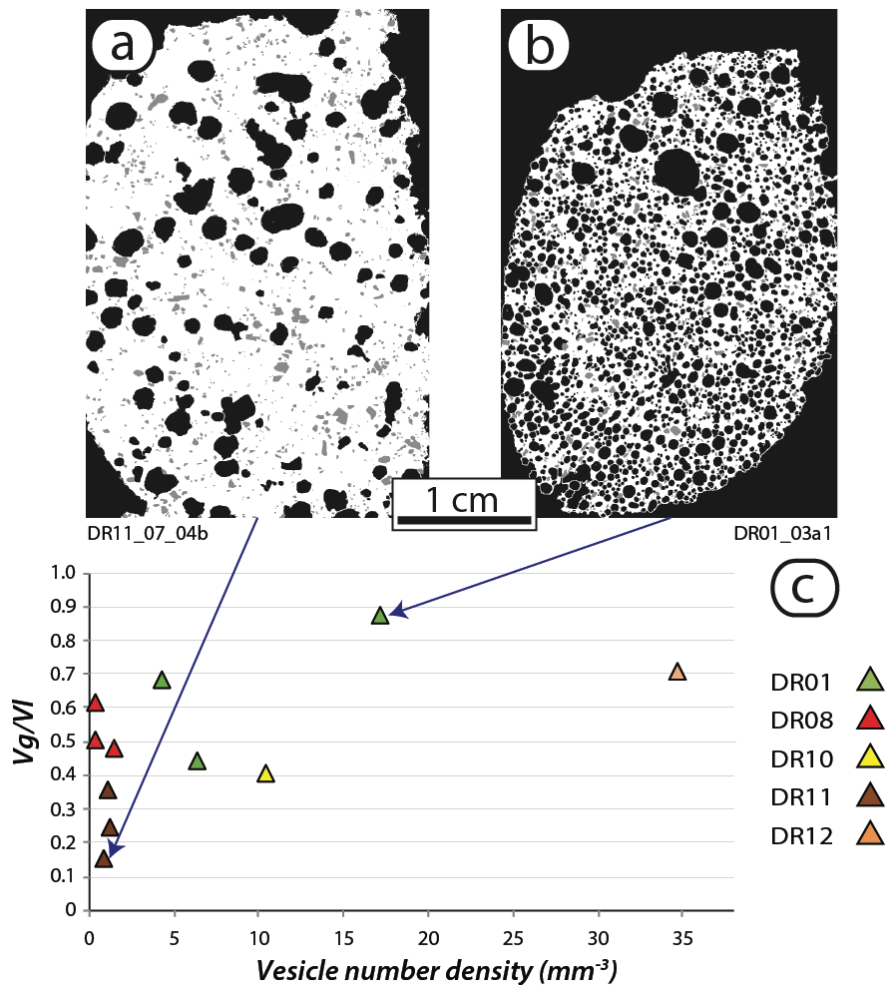
800 the cone-building phase 1 and sampled by MAYOBS 1 and 4 oceanographic cruises; DR08 and
 801 DR11 are lava flows emitted in June and July 2019 (phase 2) and sampled during Mayobs 2
 802 and 4 oceanographic cruises, respectively.



803

804 **Fig. 2:** Bulk rock geochemistry of the dredged evolved basanite lavas emitted during the 2018-
 805 2020 Mayotte eruption. a) TAS classification comparing the composition of the submarine
 806 lavas of the new edifice (Suppl. material Table 1) with that of subaerial lavas from the Comoros
 807 archipelago. Blue and green arrows show the moderately silica-undersaturated (“Karthala-
 808 trend”) and the highly silica-undersaturated (“La Grille-trend”) trends identified in Comoros
 809 lavas, respectively. b) Fractional crystallization models for Comoros and Mayotte lavas plotted
 810 in Ni (ppm) vs Mg# space. Melts in equilibrium with the mantle have a Mg# ~70 (the melting
 811 grid with mantle melting temperature and melt fractions has been computed following Späth et
 812 al., 1996)). Back calculation models start from DR0101 composition by adding in small

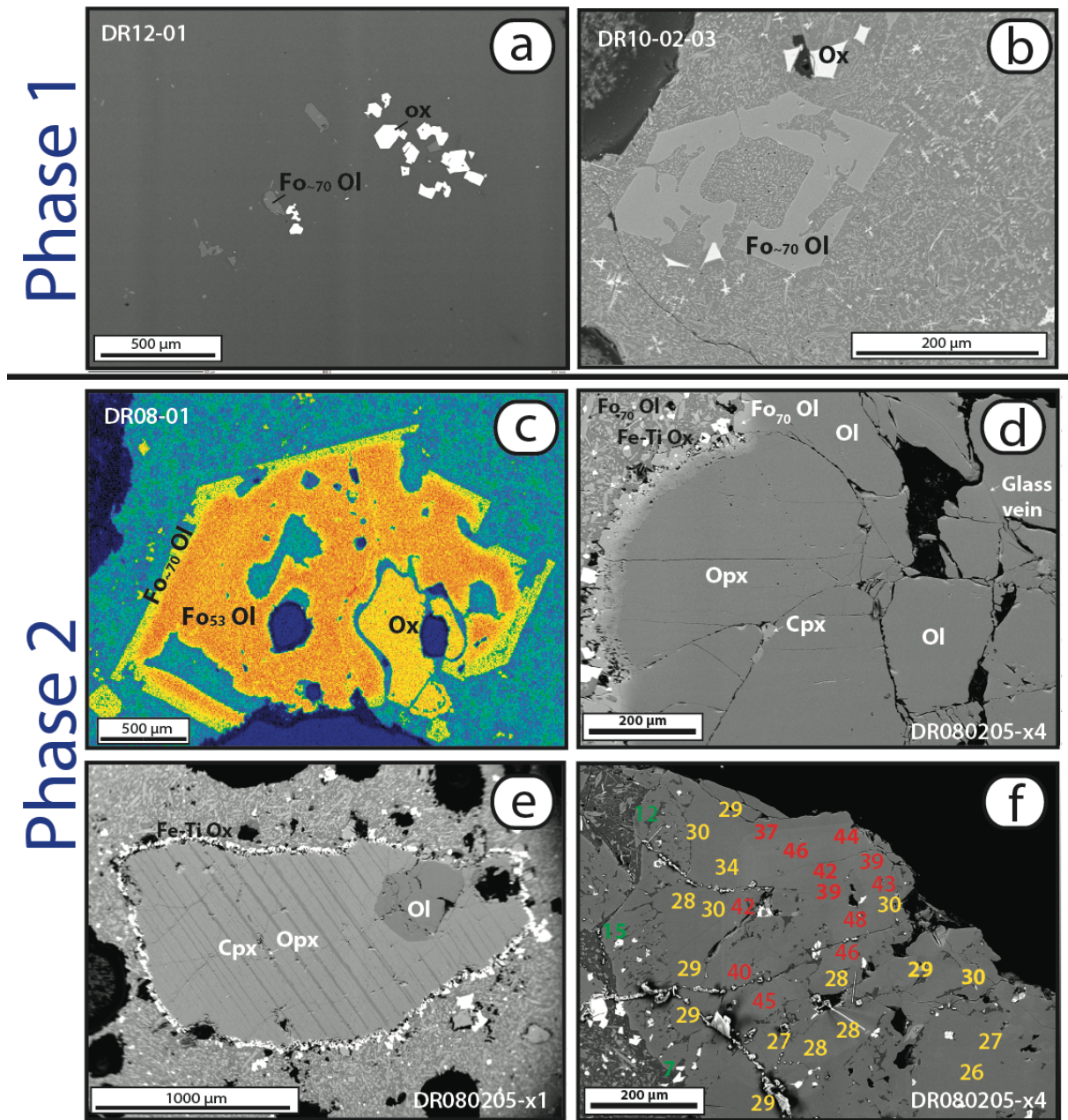
813 increments of equilibrium olivine and clinopyroxene compositions appropriate to match the
 814 composition of subaerial Comoros lavas and consistent with the Ni concentration for a primary
 815 mantle melt (300-500 ppm, Späth et al., (1996)). Olivine-only fractionation fails to reproduce
 816 the Comoros trend. c) Chondrite-normalized REE patterns of the submarine lavas of the new
 817 edifice compared to Mayotte subaerial lavas. d) La/Sm vs Sm/Yb diagram annotated with
 818 partial melting curves for garnet and spinel lherzolite mantle sources (Pouclet et al., 2016).



819

820 **Fig. 3:** Textural characteristics of the studied lava samples. Binary images of two lava
 821 fragments a) DR110704-b and b) DR0103-a1 where black = vesicles, white = glass and grey =
 822 crystals. c) Vesicle to melt ratio (Vg/Vl) vs. vesicle number density. A decrease in vesicle
 823 number density (Nv) is evident from the samples from phase 1 (DR01-DR10-DR12) to those

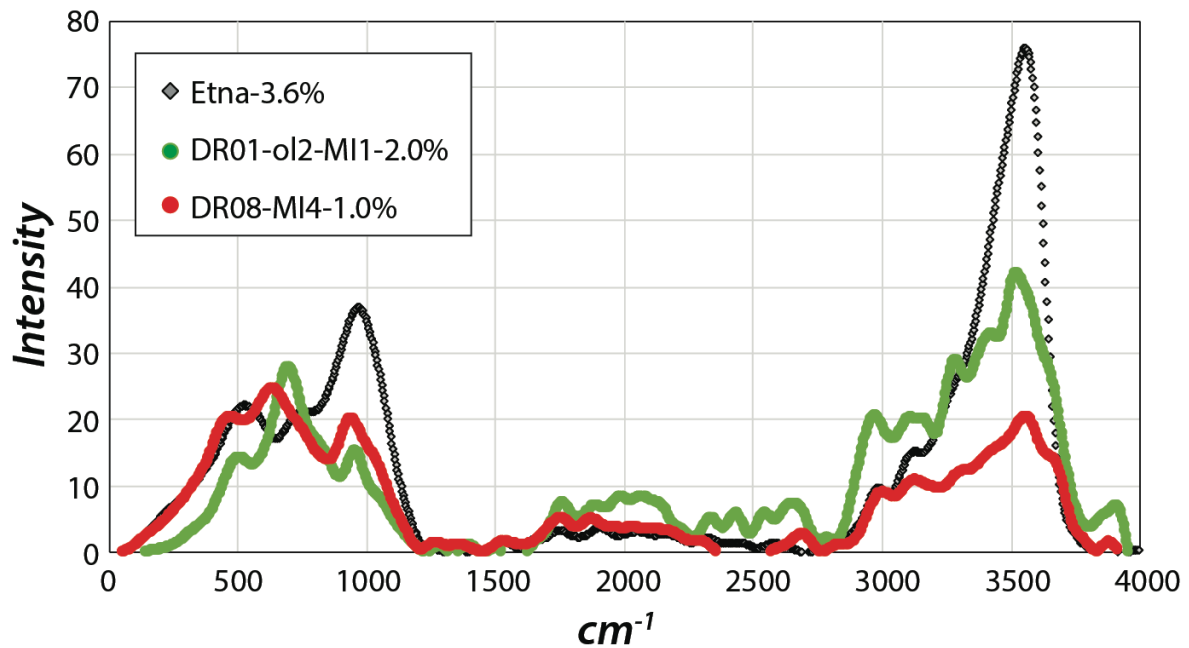
824 from phase 2 (DR08-DR11), with DR11 samples being the lowest in term of vesicularity and
 825 inferred pre-eruptive gas content.



826

827 **Fig. 4.** Petrographic features of the dredged lavas. a) All lavas have very low crystallinity: BSE
 828 image of 4 – 6% microlites of Fo_{~70} olivine (Fo_{~70} Ol, Suppl. material Table 4) and
 829 titanomagnetite (Ox) in glassy matrix of sample DR1201. b) Many crystals show textures
 830 typical of fast growth like these skeletal Fo₇₀ olivine and titanomagnetite crystals in fine-grained
 831 groundmass (sample DR100203) c) Olivine crystals in late erupted lavas (DR08; DR11) have

832 low-Fo composition (Fo₅₃) and show reverse zoning (MnO element map); these crystals are
 833 associated with large titanomagnetite crystals (ox). d) Harzburgite mantle xenolith from the
 834 later erupted lavas (sample DR080205-x4) composed of Fo₉₀ olivine and Mg_{#90} orthopyroxene
 835 (Opx); Mg_{#90-93} clinopyroxenes (Cpx) are associated with SiO₂ and K₂O-rich veins. e) Another
 836 mantle xenolith composed of a single crystal of Cpx with Opx exsolutions (sample DR080205-
 837 x1) and a few olivine and Opx crystals. f) Zoned clinopyroxene megacryst in sample
 838 DR080205-x2. Superimposed colored numbers show estimated depth of crystallization
 839 calculated through geobarometry (Putirka, 2008): red numbers are located in the low- Mg#
 840 core, yellow: high-Mg# inner rim, green: dendritic outer rim.



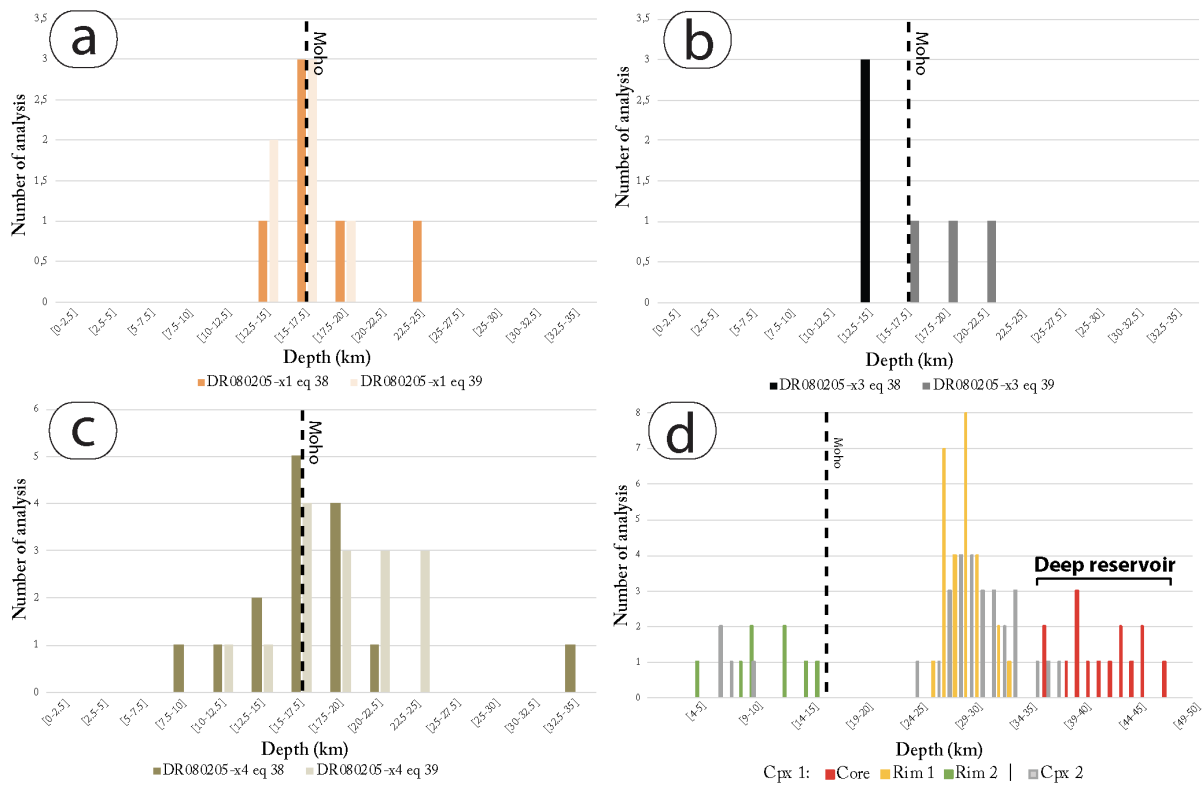
ID	DR1-03-ol2-FI1	DR1-03-ol2-MI1	DR1-03-ol3-emb	DR1-03-ol4-MI	DR8-01-MI1	DR8-01-MI2	DR8-01-MI3	DR8-01-MI4
Glass	melt inclusion	melt inclusion	embayment	melt inclusion	melt inclusion	melt inclusion	melt inclusion	melt inclusion
Host	olivine	olivine	olivine	olivine	spinel	spinel	spinel	spinel
H ₂ O	2.0	0.6	2.2	2.3	1.2	1.0	1.1	1.0

841

842 **Fig. 5** Raman spectra of an olivine-hosted melt inclusion from sample DR0103 and a spinel-
 843 hosted melt inclusion from sample DR0801 compared with reference basaltic glass containing
 844 3.6 wt% of dissolved water (Etna glass). Bands in the 100-1200 cm⁻¹ region are related to
 845 vibrations of the glass network, while the band at 3570 cm⁻¹ is produced by stretching of OH

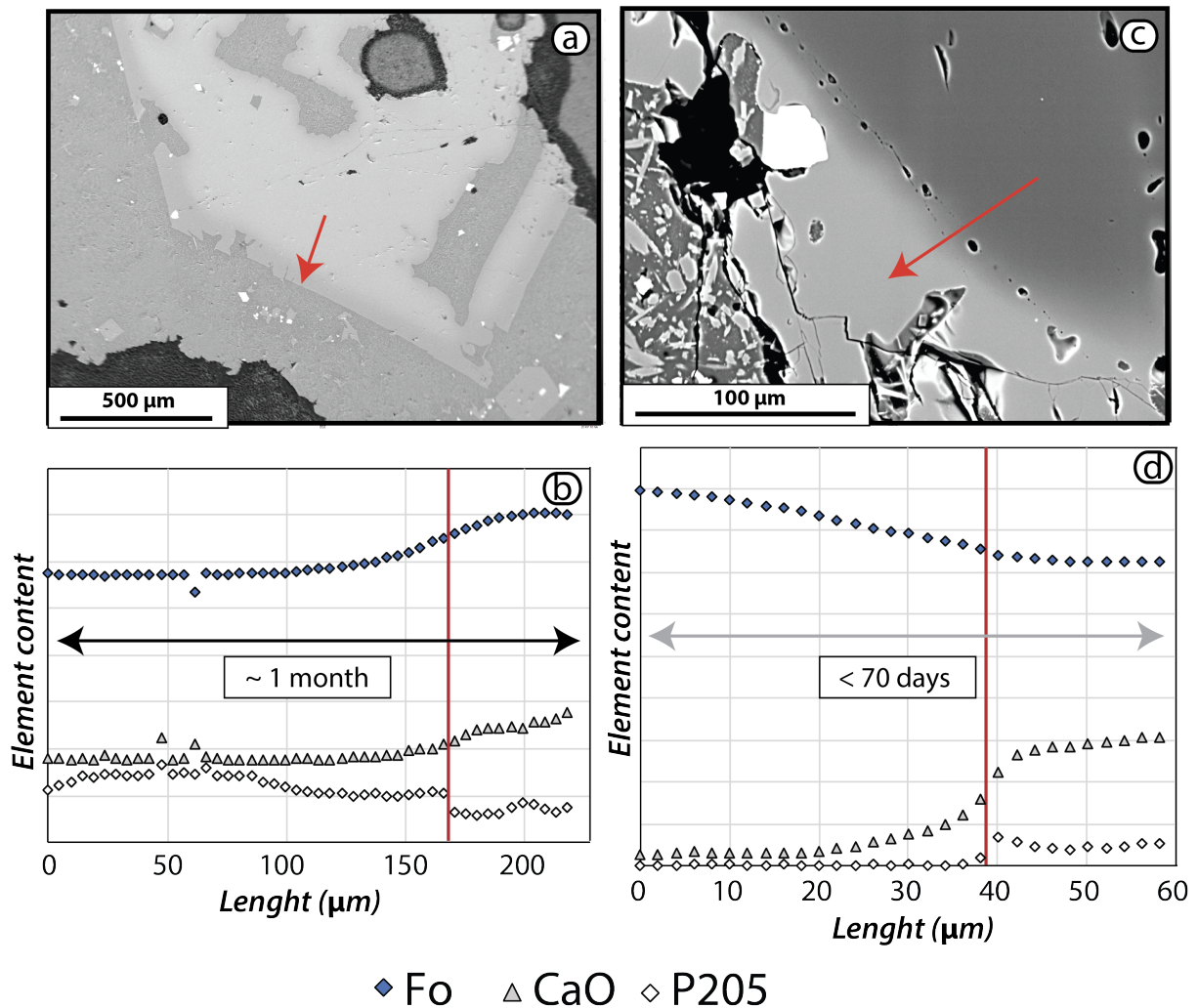
846 bonds and its intensity linearly correlates with the concentration in total dissolved water (Di
 847 Muro et al., 2006). Table shows H₂O content (wt%) in melt inclusions and embayment in
 848 DR0103 and DR0801 samples.

849



850

851 **Fig. 6:** Histograms showing depth obtained using geobarometry on clinopyroxene-
 852 orthopyroxene pairs in the mantle xenoliths in the June 2019 lava flow (DR08). The different
 853 colored bars represent results from using different equations (see discussion in text). Pyroxenes
 854 located in the three mantle xenoliths (Fig. 4d, e) were equilibrated at pressures of 0.43 ± 0.19
 855 GPa, near the depth of the Moho at 15 – 18 km (black dashed line). (a) DR080205-x1, $0.41 \pm$
 856 0.19 GPa, (b) DR080205-x3 and 0.46 ± 0.19 GPa (c) DR080205-x4; d) We obtained two
 857 additional clusters of pressures of 1.01 – 1.34 GPa and 0.62 – 0.92 GPa with a second set of
 858 geobarometry estimations using zoned clinopyroxene megacrysts (Fig. 4f). Moho is shown by
 859 a black dotted line (Dofal et al., 2018).



861

862 **Fig. 7:** Core-rim diffusion profiles in zoned olivines. Red arrows show the trace of the profiles

863 on BSE images of a) a reversely-zoned olivine in the DR0801b ALF sample, and c) a normally

864 zoned olivine in the xenolith from the DR080205x4 sample. b) and d) shows Fo, CaO and P₂O₅

865 core-rim profiles corresponding to the traces presented in a) and c) (Suppl. material Table 6).

866 The diffusion rate for P in olivine is extremely slow so this immobile element marks the initial

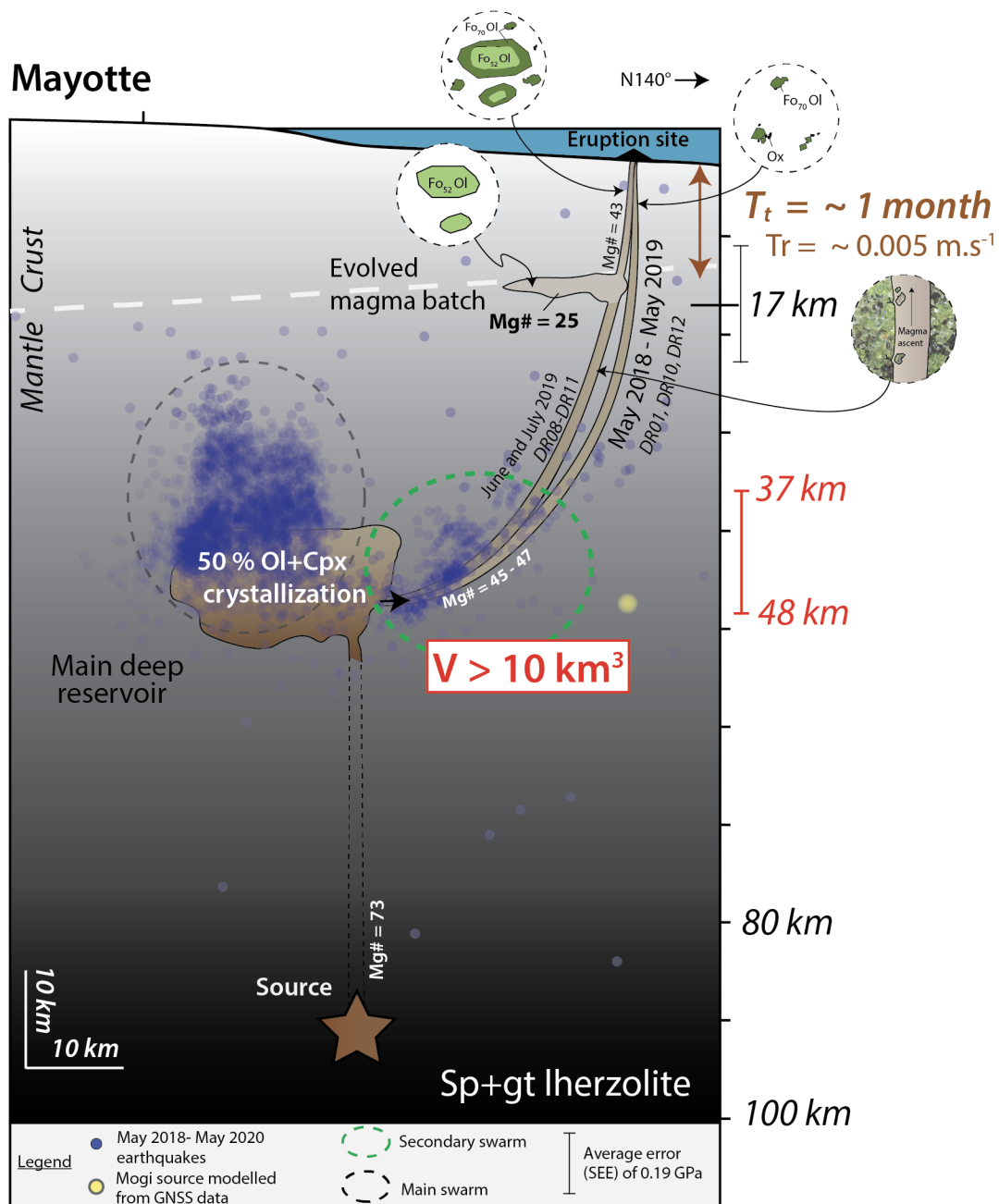
867 boundaries between zones that crystallized at different times. In the reversely-zoned phenocryst

868 of b), the initial profile was a step between a Fo₅₃ core and a Fo₇₀ rim, then Ca and Mg/Fe

869 diffused away from this initial step. In the normally zoned xenolith of d), the initial profile was

870 a step between a Fo₉₀ core and a Fo₇₂ rim, then Ca and Mg/Fe diffused away from this initial

871 step.



873

874 **Fig. 8.** Magma plumbing system feeding the 2018-2020 Mayotte eruption interpreted on the
 875 basis of petrological and geophysical data. Magma produced by partial melting of a spinel (sp)
 876 + garnet (gt) lherzolite mantle source undergoes 50% of crystallization (80% cpx + 20% ol) in
 877 a large and ≥ 37 km deep magma reservoir with a volume $\geq 10 \text{ km}^3$. Depth of this main deep
 878 storage unit constrained by barometric data is in excellent agreement with seismicity location
 879 (blue dots, ReVoSiMa, 2021) and geodetic model (yellow dot). Starting from the main deep

880 reservoir, the magma path evolved during the eruption. During the first year, eruption is fed by
 881 direct ascent of magma from the deep reservoir to the surface through NW-SE lithospheric
 882 structures. The shape and the size of microlites indicate that most micro-crystallization occurred
 883 in the shallow part of the ascending dyke. A shallower and smaller differentiated magma
 884 reservoir located close to the Moho ($< 17 \pm 6$ km) was sampled *en route* during the second year
 885 of the eruption. It is important to note that this magma batch and the shallow conduit were not
 886 imaged by on-land seismometers because they are located too far from the eruption site to allow
 887 identification of small, shallow earthquakes. Moho: grey dotted line (Dofal et al., 2018). Tt:
 888 Transfer time, Tr: Transfer rate = distance / transfer time, V: volume.

889

890 **Table captions**

891

Dredges	Oceanographic cruise	DOI : 10.18142/291	Start dredging			End dredging		
			Latitude	Longitude	Depth	Latitude	Longitude	Depth
DR01	MAYOBS 1	10.17600/18001217	12°54.30' S	45°43.13' E	3050 m	12°54.51' S	45°43.08' E	2820 m
DR08	MAYOBS 2	10.17600/18001222	12°56.46' S	45°42.88' E	3072 m	12°56.05' S	45°41.91' E	3050 m
DR10	MAYOBS 4	10.17600/18001238	12° 54.94' S	45° 43.31' E	3120 m	12° 55.05' S	45°43.24' E	2950 m
DR11	MAYOBS 4	10.17600/18001238	12°54.80' S	45°41.57' E	3250 m	12°55.20' S	45°41.55' E	3228 m
DR12	MAYOBS 4	10.17600/18001238	12°52.90' S	45°42.94' E	3245 m	12°52.97' S	45°42.93' E	3200 m

892

893 **Tab. 1:** Location of dredges performed during MAYOBS 1 (DR01), MAYOBS 2 (DR08) and
 894 MAYOBS 4 (DR10, DR11 and DR12) oceanographic campaigns. No dredges were performed
 895 during MAYOBS 3.

896

897